



This is a repository copy of *Coupling depth-averaged and 3D numerical models for the simulation of granular flows*.

White Rose Research Online URL for this paper:

<https://eprints.whiterose.ac.uk/190236/>

Version: Accepted Version

Article:

Pasqua, A., Leonardi, A. and Pirulli, M. (2022) Coupling depth-averaged and 3D numerical models for the simulation of granular flows. *Computers and Geotechnics*, 149. 104879. ISSN 0266-352X

<https://doi.org/10.1016/j.compgeo.2022.104879>

© 2022 Elsevier Ltd. This is an author produced version of a paper subsequently published in *Computers and Geotechnics*. Uploaded in accordance with the publisher's self-archiving policy. Article available under the terms of the CC-BY-NC-ND licence (<https://creativecommons.org/licenses/by-nc-nd/4.0/>).

Reuse

This article is distributed under the terms of the Creative Commons Attribution-NonCommercial-NoDerivs (CC BY-NC-ND) licence. This licence only allows you to download this work and share it with others as long as you credit the authors, but you can't change the article in any way or use it commercially. More information and the full terms of the licence here: <https://creativecommons.org/licenses/>

Takedown

If you consider content in White Rose Research Online to be in breach of UK law, please notify us by emailing eprints@whiterose.ac.uk including the URL of the record and the reason for the withdrawal request.



eprints@whiterose.ac.uk
<https://eprints.whiterose.ac.uk/>

Coupling Depth-Averaged and 3D numerical models for the simulation of granular flows

Andrea Pasqua^{a,1}, Alessandro Leonardi^{b,2} and Marina Pirulli^a

^aPolitecnico di Torino, Corso Duca degli Abruzzi 24, Torino, 10129, Italy

^bThe University of Sheffield, Western Bank, Sheffield, S10 2TN, United Kingdom

ARTICLE INFO

Keywords:

Granular flows
Depth-Averaged Method
3D Lattice-Boltzmann Method
Coupled Method
Hazard mitigation

ABSTRACT

Continuum-based numerical models are widely used to simulate debris flows due to their reliability in predicting the movement path, depth and velocity, which are key parameters to design mitigation structures. Nowadays, two main families of continuum-based models exist: depth-averaged (DA) models and three-dimensional (3D) models. If the former are already able to determine the key flow parameters, only the latter allow a detailed investigation of a flow-structure interaction. The study of the whole propagation path with a 3D model would be extremely complex and time-consuming, but the whole process influences the flow-structure interaction. Therefore, this work aims to couple a DA model and a 3D model (DA-3D). The first model simulates the flow in the upper part of the propagation path, where no structure exists. The second model takes over upstream of the structure to be analysed. At the transition from one model to the other, the coupling requires that outputs of the DA model become inputs of the 3D model. The validation of the DA-3D model is made through numerical simulations of the experimental results obtained on a flume apparatus at laboratory scale. The obtained numerical results confirmed the successful coupling of the two models.

1. Introduction

Debris flows are among the most hazardous landslide phenomena occurring worldwide, mainly affecting mountain communities. They consist of fine and poorly-sorted coarse material, saturated with water (RM Iverson, 1997; Chien-Yuan et al., 2005; Nikolopoulos et al., 2015) flowing in channelised paths (Coussot and Meunier, 1996). Common features are the absence of premonitory signs, high speed and long runout (Marchi et al., 2002; Hürlimann et al., 2003; Winter et al., 2006). Due to their high velocity and unpredictability, the evacuation of the local population is often difficult to operate, with casualties (García-Delgado et al., 2019; Larsen et al., 2001) and economic damage likely to occur (Winter et al., 2016).

Risk assessment procedures are often carried out (Wu et al., 1996). In particular, the generation of quantitative hazard maps has helped to mitigate risk in many areas prone to debris flows and, more generally, to landslide risk. To reduce risk, the use of filter barriers such as slit dams (Fig. 1), cable net barriers (Leonardi et al., 2016) or rack dams (Leonardi and Pirulli, 2020) is an effective strategy. Their primary task is to reduce the flow energy (Canelli et al., 2012; Song et al., 2017), and to retain the largest boulders (Takahashi, 2007; Wendeler et al., 2007; Leonardi and Pirulli, 2020; Leonardi et al., 2021).

A rational, computer-aided method to design these structures is still under development. The major issues are related to a poor understanding of the flow rheology (Iverson, 2003) and of its interaction with solid obstacles (RM Iverson, 1997). Hence, to improve the barrier design, it is necessary to gain better understanding of (i) debris flow dynamics,

and (ii) flow-structure interaction. The study of debris flow dynamics and flow-structure interaction can be conducted with physical or numerical models. Physical models can be assembled either at the laboratory scale or in large-scale facilities. While the former (Scheidl et al., 2013; Choi et al., 2018) requires a difficult scaling of all physical variables (Iverson, 2015), the latter (Major, 1997) demands considerable investment, and often only a few experimental realisations can be conducted. Numerical models are a valid and powerful alternative to physical models. They are not directly affected by scale effects, and require fewer economic resources, with simulations that are repeatable with no limits linked to material availability.

Nowadays, a wide number of numerical models can model the dynamic of debris flows, either under discrete or continuum assumptions. The discrete element method (DEM) treats flows as assemblies of colliding particles. DEM has been successfully employed (Cleary and Sawley, 2002; Stolz and Huggel, 2008; Li and Zhao, 2018; Shen et al., 2018), but the total number of particles that can be simulated is limited. Continuum-based numerical approaches can overcome this limitation and several models have been proposed, both in depth-averaged (DA) and three-dimensional (3D) forms.

DA and 3D models are based on rather different hypotheses. DA models depth-average the mass and momentum conservation equations, and thus information along the vertical direction is averaged. This procedure leads to quick and reliable analyses of flow propagation. However, since the information along the vertical direction is averaged, the flow-structure interaction might be over-simplified. On the contrary, 3D models can compute the internal shear deformation and all three velocity components along the

✉ andrea.pasqua@polito.it (A. Pasqua)
ORCID(s): 0000-0002-6089-4857 (A. Pasqua)



Figure 1: Example of filter barrier, Saint-Vincent, Aosta Valley (Italy).

flow depth. Nevertheless, studying the whole phenomenon in 3D would be extremely time-consuming and complex.

Among others (Pastor et al., 2015; Zhan et al., 2019; Dunatunga and Kamrin, 2015; Yue et al., 2015) the Lattice Boltzmann Method (LBM) is a relatively recent 3D continuum fluid solver that can be employed to study flow-structure interaction problems. LBM is a valid candidate to perform 3D analyses and thus to compute accurate flow representations including impact forces. In the last two decades, LBM has increased in popularity in numerical modelling. It has become a valid alternative to more classic computational fluid dynamics solvers (CFD). In particular, it can treat complex geometries (Succi et al., 1989; Mazzeo and Coveney, 2008; Adhianto et al., 2010) without significant losses in performance. Moreover, parallel computing is easier to implement compared to more classic CFD solvers (Desplat et al., 2001; Mazzeo and Coveney, 2008). Therefore, the computational time required to run complex analyses may be reduced (Kandhai et al., 1998; Desplat et al., 2001; Harting et al., 2005; Kazemian et al., 2018). Furthermore, multiphase flows (such as debris flows) can be treated in LBM (Li and Zhao, 2018; He et al., 1999; McCracken and Abraham, 2005; Premnath and Abraham, 2007).

This paper aims to study the flow-structure interaction with a 3D model without neglecting to study the upstream propagation phase of debris flows. Hence, a coupled DA-3D model is proposed, where LBM is the 3D solver of choice. The upper part of the propagation phase, where it is assumed that no structure is present, is studied with a DA model. Once the flow approaches a structure, the DA variables are used by a 3D model to study the remaining part of the flow path, which includes flow-structure interaction as well. Fig. 2 illustrates how the two methods are combined, with a coupling section that splits the domain into two parts. This coupling of DA and 3D can optimise the computational time while allowing for a full resolution of flow-structure interaction on realistic topographies.

Three elements of novelty are proposed in this paper: (i) an implementation of a frictional rheology in LBM, (ii) an inlet condition for free-surface granular flows, and (iii) the coupling algorithm. The paper is organised as follows. Section 2 describes the rheologies used in the depth-averaged and 3D models employed in this paper. Section 3 describes the model proposed in this work. The coupling algorithm is also discussed. In Section 4 a frictional rheology for LBM on a benchmark geometry is validated, and in Section 4.2 the inlet condition for the 3D model is discussed. Finally, Section 5 is dedicated to the validation of the coupled model by back-calculating a model flow obtained in a laboratory flume and some preliminary considerations regarding the computing efficiency are proposed.

2. A frictional rheology for depth-averaged and three-dimensional methods

At a first approximation, debris flows are modelled as dense granular flow. Among the multiple laws used to describe this state, the $\mu(I)$ rheology (Jop et al., 2005; Lagrée et al., 2011), is becoming increasingly popular. This is thanks to its solid empirical background, and its ability to quantitatively predict granular flows under various conditions, such as the granular column collapse (Lagrée et al., 2011), the outflow from a silo (Staron et al., 2014), and others (GDR MiDi, 2004).

Formulations for the $\mu(I)$ rheology have been reported both in local form and in depth-averaged form. The former can be employed in 3D frameworks, while the latter can be used in DA frameworks.

Regardless of the form, the $\mu(I)$ rheology can be seen as a generalisation of the Coulomb friction model. The ratio between shear stress τ and confinement pressure p originates a friction coefficient μ which is not constant, but, rather, depends on a local dimensionless parameter, the inertial number I :

$$\mu(I) = \frac{\tau}{p}. \quad (1)$$

The inertial number can be seen as the ratio between the timescale of particle rearrangement during flow and that of shear deformation (GDR MiDi, 2004; Jop et al., 2006):

$$I = \frac{d}{\sqrt{p/\rho_p}} \dot{\gamma}, \quad (2)$$

where ρ_p is the particle density and $\dot{\gamma}$ is the shear rate. A low value of I leads to quasi-static behaviour, while high values of I correspond to a rapid flow (GDR MiDi, 2004). Due to this, several researchers investigated the dependence of μ on I , both in DA and 3D frameworks.

It is important to stress that the $\mu(I)$ rheology is based on the assumption of mono-dispersed particles, where a single diameter of the particles is used to define the inertial number (Eq. 2). In case of non-uniform particles, the $\mu(I)$ rheology

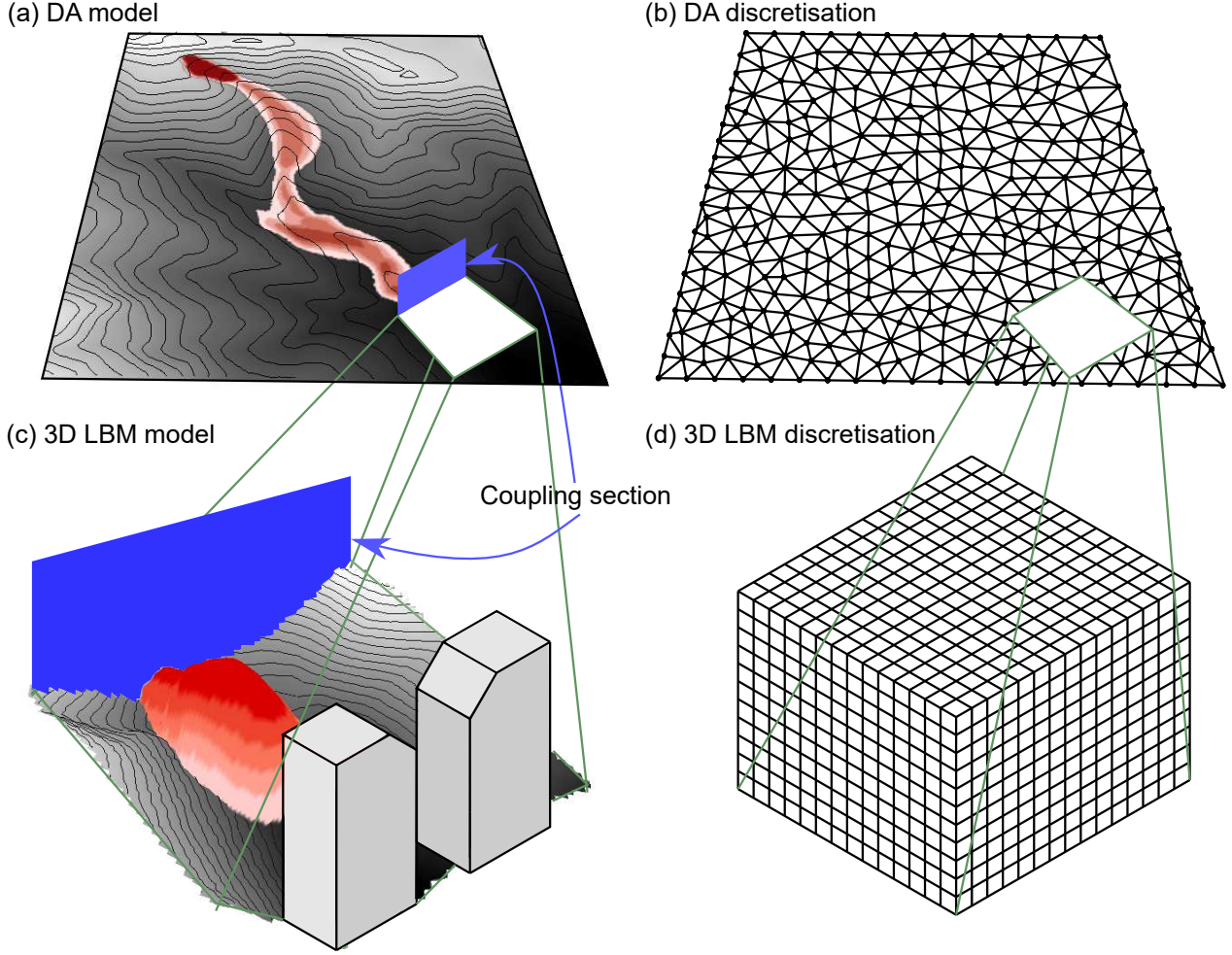


Figure 2: General scheme to couple DA and 3D models. Topography and flow are represented by greyscale and red colours respectively. A depth-averaged resolution flow (a) with its discretisation (b). A 3D flow resolution (c) with its discretisation (d).

should be reformulated, although some authors do use the basic $\mu(I)$ rheology even for bi-dispersed flows (Trehela and Ancy, 2021).

In the DA framework, steady-uniform flows over planes inclined of an angle θ have been widely studied (Pouliquen, 1999; Pouliquen and Forterre, 2002). It was observed that a steady-state is reached if the slope angle θ is within two critical values: $\mu_s = \tan \theta_s$ and $\mu_d = \tan \theta_d$ which are the static and dynamic friction coefficient, respectively. In these conditions, gravity and friction are in equilibrium. When $\theta < \theta_s$ no flow is possible since the frictional forces prevail. For $\theta > \theta_d$ the flows accelerate indefinitely since the gravitational acceleration prevails over frictional forces.

Experimental evidence (Pouliquen, 1999; Pouliquen and Forterre, 2002) links μ to the flow depth h , and to the Froude number $Fr = \bar{u}/\sqrt{gh \cos \theta}$ where \bar{u} is the depth-averaged velocity, and g is gravity:

$$\mu(Fr, h) = \mu_s + \frac{\mu_d - \mu_s}{\frac{\beta h}{Ld} \frac{1}{Fr} + 1}. \quad (3)$$

In this expression, which is visually represented by Fig. 3, β is a dimensionless constant, L is a dimensionless parameter linked to the flow thickness (Pouliquen, 1999), and d is the particle diameter. It must be highlighted that in Eq. 3 μ is a function of depth-averaged values. Hence, the expression governs the basal resistance.

To extend the formulation beyond uniform conditions, Jop et al. (2005) generalised the μ rheology to a 3D framework, with I a local parameter, function of local state variables. In analogy to the depth-average theory, in steady-uniform flows I is constant, and velocity follows a Bagnold profile (GDR MiDi, 2004), leading to:

$$\bar{u} = \frac{2I}{5d} \sqrt{\Phi g \cos \theta} h^{3/2}, \quad (4)$$

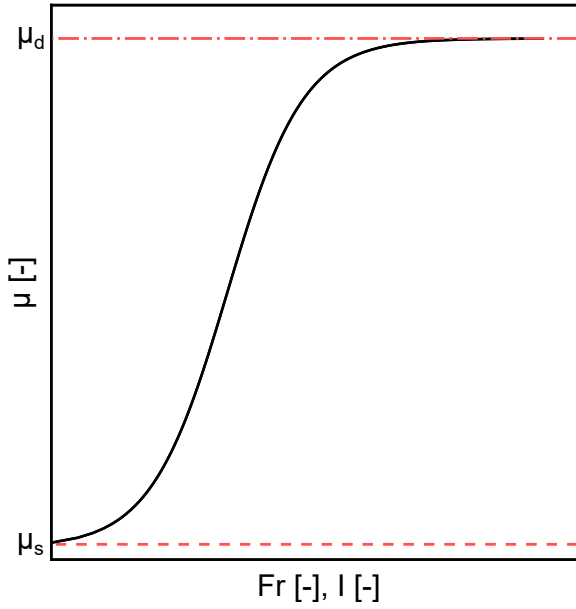


Figure 3: Friction coefficient μ as a function of the Froude number Fr .

where Φ is the solid volume fraction, which for dense flows can be assumed within the range 0.50-0.60 (GDR MiDi, 2004; Chialvo et al., 2012; Jop, 2015). Thus, by substituting Fr and \bar{u} in Eq. 3, one obtains the local form of μ :

$$\mu(I) = \mu_s + \frac{\mu_d - \mu_s}{\frac{I_0}{I} + 1}, \quad (5)$$

where the constant I_0 (Gray and Edwards, 2014) is:

$$I_0 = \frac{5\beta}{2L\sqrt{\Phi}}. \quad (6)$$

Therefore, two equivalent expressions of the $\mu(I)$ rheology are available: a depth-average version and a local one.

It must be emphasised that the local expression of $\mu(I)$ is derived from the depth-averaged framework. Hence, when coupling a DA and a 3D model, no inconsistencies from a rheological point of view are present, provided that the two versions are implemented with equivalent parameters. The depth-averaged $\mu(I)$ rheology is based on μ_s , μ_d , β , L , and d . Once the DA model is calibrated, its rheological parameters can be used to obtain those of the local $\mu(I)$. The parameters μ_s and μ_d appear in both versions and have the same physical meaning, while ρ_p , and d are known material parameters. I_0 can be calculated from Eq. 6

2.1. Regularisation of the local $\mu(I)$ rheology

In a local form, the ratio between the shear stress and the shear rate yields an expression for the apparent dynamic viscosity (Jop et al., 2006) which, for the $\mu(I)$ rheology,

reads:

$$\nu = \frac{\tau}{\dot{\gamma}\rho} = \frac{\mu(I)p}{\dot{\gamma}\rho} = \left(\mu_s + \frac{\mu_d - \mu_s}{\frac{I_0}{I} + 1} \right) \frac{p}{\dot{\gamma}\rho}. \quad (7)$$

If $\dot{\gamma}$ tends to zero, e.g. when approaching static conditions, the viscosity diverges, which is physically inconsistent. Furthermore, at the free surface both $|\dot{\gamma}|$ and p vanish, leading to an indeterminate value of ν . This is a known issue (Barker et al., 2015), which is usually mitigated by adopting a regularisation scheme. This work adopts the regularisation proposed by Franci and Cremonesi (2019) who discussed two alternative algorithms to regularize viscosity: (i) exponential and (ii) penalty. This paper employs the exponential method since its implementation in the 3D model of choice is more suitable. Thus, the viscosity expression becomes:

$$\nu = \frac{p}{\dot{\gamma}\rho} \left[\mu_s \left(1 - \exp\left(\frac{-\dot{\gamma}}{\lambda}\right) \right) + \frac{\mu_d - \mu_s}{\frac{I_0}{I} + 1} \right], \quad (8)$$

where λ is a regularisation parameter. Dimensionally, $1/\lambda$ is a time. Note that in 8 for $\lambda \rightarrow 0$ one obtains:

$$\lim_{\dot{\gamma} \rightarrow 0} \nu = \frac{p}{\rho} \left[\frac{\mu_s}{\lambda} + \frac{\mu_d - \mu_s}{\frac{I_0}{I} + 1} \right], \quad (9)$$

which is coherent with the theory (Jop et al., 2005; GDR MiDi, 2004; Lagr e et al., 2011). Eq. 9 is the lower limit that the viscosity can reach, and thus no cut-off has to be applied.

3. The coupled numerical model

3.1. Multi-domain strategy

It is assumed that the medium is homogeneous and incompressible, and employs a single-phase approximation for both DA (Savage and Hutter, 1989) and 3D model (Mohamad, 2011). Furthermore, it is assumed that the solid particles are much smaller than the flow depth and length (Pirulli and Mangeney, 2008). With these conditions met, an equivalent fluid whose characteristics reasonably approximate the real flow can usually be found (Fig. 4), and the mass and momentum balance can be written as:

$$\nabla \cdot \mathbf{u} = 0, \quad (10)$$

$$\rho \left(\frac{\partial \mathbf{u}}{\partial t} + \mathbf{u} \nabla \cdot \mathbf{u} \right) = \nabla \cdot \boldsymbol{\sigma} + \rho \mathbf{g}. \quad (11)$$

In the DA framework, this set of equations is averaged. Savage and Hutter (1989) were the first authors to propose a DA model for granular flows. Due to its hyperbolicity, their original set of equations is known to have issues in handling

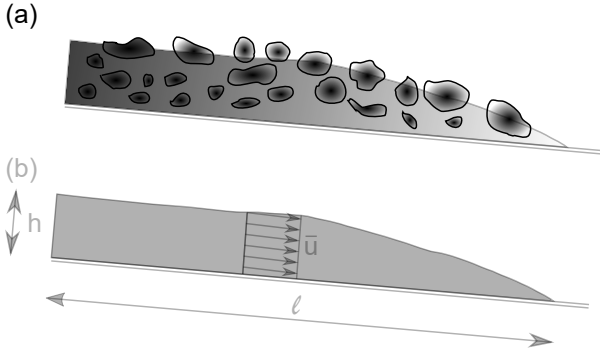


Figure 4: (a) Debris representation as a liquid-solid mixture. (b) Equivalent fluid approximating the real flow features.

large gradients of the physical variables (e.g. shock waves, velocity change from supercritical to subcritical). These are known to occur when a granular flow impacts an obstacle.

The research community has addressed this problem by using the so-called high-resolution methods. One of the most implemented high-resolution methods is the non-oscillatory central differencing scheme with limiters and cell reconstruction algorithms. Describing and listing high-resolution methods would go beyond the goal of this paper. The interested reader is redirected towards Pudasaini and Hutter (2003); Tai (2000); Tai et al. (2002); Wang et al. (2004); Pudasaini et al. (2005); Chiou et al. (2005).

Although these approaches are powerful and consistent, in this paper what may be a more flexible and promising alternative is proposed. Instead of modifying the numerical scheme in the DA model of choice, its use is limited to when the flow is far from a structure. As soon as the flow approaches an obstacle, a 3D model is applied. This allows us to study vertical acceleration and shock waves. Furthermore, the flow-structure interaction can be studied point by point without depth-averaging physical quantities such as pressure and velocity, and without resorting to *ad hoc* solutions.

Fig. 2 depicts how the coupled model is envisioned. A coupling section (the vertical blue area in the figure) splits the domain into two regions. In the first region (grey-coloured in Fig. 2(a)), it is assumed that no structure is present in the flow path. This part of the domain is solved with a DA model. Whereas in the second region (grey-coloured in Fig. 2(b)), structure and obstacles are present in the flow path. The 3D LBM model is employed to carry out the analyses in this region.

The following sections discuss how DA and 3D LBM solve Eqs. 10 and 11 to model granular flows, and the proposed coupling algorithm.

3.2. 2D domain: depth-averaged model (DA)

A complete description of the DA framework would be beyond the goals of this paper. The interested reader is redirected towards Mangeney-Castelnau (2003), or Pirulli and Mangeney (2008) for a more practical approach. However, the most relevant features are briefly described here.

During a granular flow event, the runout length ℓ is much larger than the flow depth h , as illustrated in Fig. 4(b). This approximation is employed in the derivation of DA models (Savage and Hutter, 1989; Hutter et al., 1995; RM Iverson, 1997; Douady et al., 1999; Jenkins and Askari, 1999; Iverson and Denlinger, 2001; Mangeney-Castelnau, 2003). Thus, the generalised Saint-Venant equations are obtained from Eqs. 10 and 11 (Savage and Hutter, 1989). Since collisions and shearing are assumed to be localised at the interface between flow and topographic surface (Kilburn, 1998), a suitable basal resistance law is necessary (Pirulli and Mangeney, 2008). This is typically a Coulomb-like law. However, Naef et al. (2006) discussed other possibilities.

This work employs a non-commercial DA software, which has been widely validated (Pirulli, 2005; Pirulli et al., 2007). The DA assumes a reference frame linked to the topography, and isotropy of normal stresses. Thus, the depth-averaged form of Eqs. 10 and 11 reads:

$$\frac{\partial h}{\partial t} + \frac{\partial(h\bar{u})}{\partial x} + \frac{\partial(h\bar{v})}{\partial y} = 0, \quad (12)$$

$$\frac{\partial(h\bar{u})}{\partial t} + \frac{\partial(h\bar{u}^2)}{\partial x} + \frac{\partial(h\bar{u}\bar{v})}{\partial y} = g_x h - \frac{\partial}{\partial x} \left(g_z \frac{h^2}{2} \right) - \mu g_z h \frac{\bar{u}}{\|\bar{\mathbf{u}}\|}, \quad (13)$$

$$\frac{\partial(h\bar{v})}{\partial t} + \frac{\partial(h\bar{u}\bar{v})}{\partial x} + \frac{\partial(h\bar{v}^2)}{\partial y} = g_y h - \frac{\partial}{\partial y} \left(g_z \frac{h^2}{2} \right) - \mu g_z h \frac{\bar{v}}{\|\bar{\mathbf{v}}\|}, \quad (14)$$

where \bar{u} and \bar{v} represent the depth-averaged velocity components in x and y , respectively, h is the flow depth, μ is the coefficient that simulates the resistance to flow introduced in Section 2. The formulation of μ depends on the rheology. Since in this paper the application is confined to a granular flow at the laboratory scale, the rheology proposed by Pouliquen (1999) (see Section 2) is employed. Therefore, μ in Eq. 13 and 14 assumes the form reported in the Eq. 3.

3.3. 3D domain: Lattice-Boltzmann method

Contrary to DA, LBM does not directly solve Eqs. 10 and 11 but rather lays its foundation on the kinetic theory, and on the Boltzmann equation (Arkeryd, 1972; Cercignani C., 1988; He and Luo, 1997). The internal mechanics rely on a mesoscopic kinetic description of the fluid as a collection of streaming and colliding particles. Macroscopic quantities, such as velocity and pressure, are reconstructed starting from the results of the microscopic processes. Conservation of mass and momentum is imposed, and a mechanism for viscous dissipation of energy is introduced. Therefore, each realisation of LBM is equivalent to a solution of Eqs. 10 and 11. The principles governing LBM are recalled here for completeness. However, a complete description would go beyond the scope of this work. The interested reader is

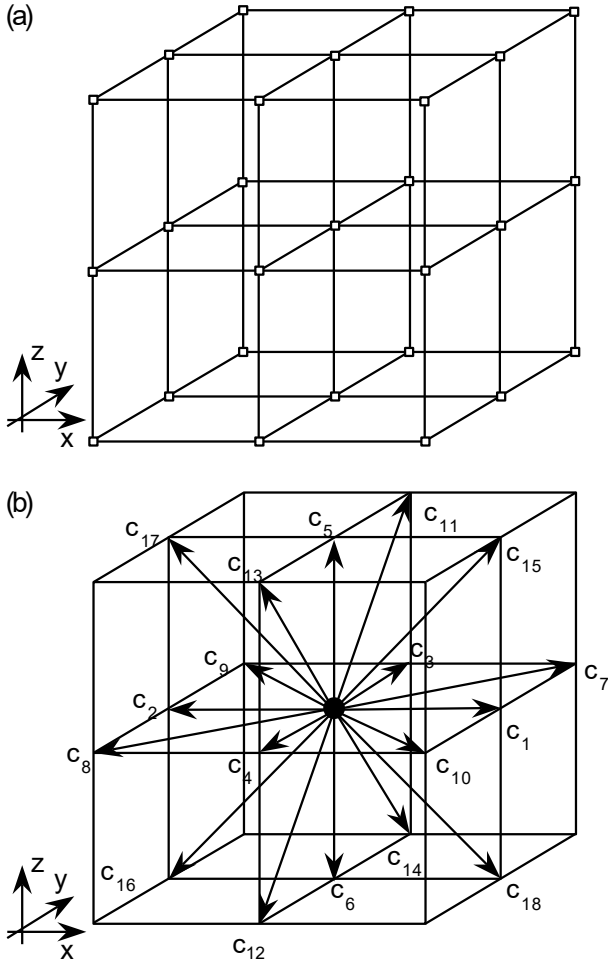


Figure 5: Lattice used for discretising variables in LBM: (a) regular grid; (b) discrete velocities.

redirected towards Succi (2003), or to Mohamad (2011) for a more practical approach.

The variable of choice is a probability density function $f(\mathbf{x}, t, \mathbf{c})$, representing the probability of finding fluid particles with speed c at location \mathbf{x} and time t . In LBM, space is discretised using a regular grid, or lattice, with unitary spacing as depicted in Fig. 5. Moreover, the microscopic velocity field is also discretised, with only a small subset of velocities allowed. Each velocity represents the movement from one lattice node to one of the eligible neighbours, as represented in Fig. 5. This work employs a 3D lattice with 19 permitted velocities \mathbf{c}_i , the so-called D3Q19 lattice:

$$\mathbf{c}_i = \Delta S / \Delta t \cdot \begin{cases} (0, 0, 0) & \text{for } i = 0, \\ (\pm 1, 0, 0) & \text{for } i = 1 \div 2, \\ (0, \pm 1, 0) & \text{for } i = 3 \div 4, \\ (0, 0, \pm 1) & \text{for } i = 5 \div 6, \\ (\pm 1, \pm 1, 0) & \text{for } i = 7 \div 10, \\ (0, \pm 1, \pm 1) & \text{for } i = 11 \div 14, \\ (\pm 1, 0, \pm 1) & \text{for } i = 15 \div 18, \end{cases} \quad (15)$$

which is a suitable scheme to solve fluid dynamics, since it offers good performance and accuracy. Δt is the time step,

and $\Delta S = \Delta x = \Delta y = \Delta z$ in LBM is the lattice discretisation. The discretised form of the probability density function reads $f_i(\mathbf{x}, t)$, with i indicating the respective discrete velocity. Macroscopic quantities, such as velocity, density, and pressure, are reconstructed through simple summation:

$$\rho = \sum_{i=0}^{18} f_i, \quad (16)$$

$$\mathbf{u} = \sum_{i=0}^{18} f_i \mathbf{c}_i / \rho, \quad (17)$$

$$p = c_s^2 \cdot \rho, \quad (18)$$

where ρ , \mathbf{u} , and $c_s = \frac{1}{\sqrt{3}} \cdot \frac{\Delta S}{\Delta t}$ are the fluid density, fluid velocity, and the lattice speed of sound (Mohamad, 2011), respectively. LBM treats the fluid as a slightly compressible medium, with pressure linked to the density fluctuations.

The equation governing the evolution of f is a discretised form of the Boltzmann equation:

$$f_i(\mathbf{x} + \mathbf{c}_i, t + 1) = f_i(\mathbf{x}, t) + \Omega_{\text{coll},i}(\mathbf{x}, t), \quad (19)$$

where Ω_{coll} is an operator reproducing the effect of microscopic collisions. In this paper, the form of Eq. 19 follows the BGK approach (Bhatnagar et al., 1954), i.e. the collision operator simply drags the system towards thermodynamic equilibrium:

$$\Omega_{\text{coll},i} = \frac{f_i^{\text{eq}} - f_i}{t_r} \Delta t, \quad (20)$$

where t_r is the relaxation time. f_i^{eq} is the probability density function at equilibrium, which for a specific value of macroscopic velocity and density is:

$$f_i^{\text{eq}}(\mathbf{u}, \rho) = \rho w_i \left(1 + \frac{\mathbf{c}_i \mathbf{u}}{c_s^2} + \frac{(\mathbf{c}_i \mathbf{u})^2}{2c_s^4} - \frac{\mathbf{u} \mathbf{u}}{2c_s^2} \right). \quad (21)$$

The set of weights w_i ensures that the equilibrium distributions also obey Eqs. 16 and 17. The w_i values for the lattice of choice (Fig. 5) are:

$$w_i = \begin{cases} 12/36 & \text{for } i = 0, \\ 2/36 & \text{for } i = 1 \div 6, \\ 1/36 & \text{for } i = 7 \div 18. \end{cases}$$

Finally, to track the position of the free surface, a volume of fluid method (Körner et al., 2005) is applied.

To implement the $\mu(I)$ rheology in LBM, the relaxation time t_r can be directly related to the fluid viscosity ν as:

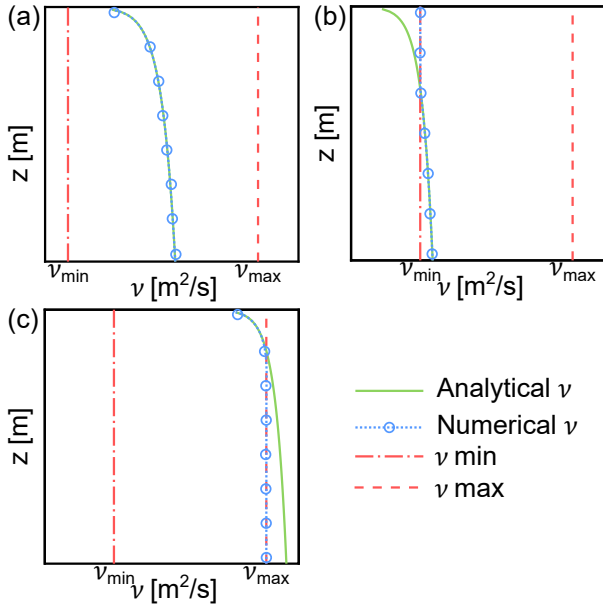


Figure 6: Analytical Lagr ee et al. (2011) and numerical viscosity ν for $\mu(I)$ rheology with LBM cut-off ν_{\min} and ν_{\max} . (a) Correct lattice and time step discretisation. (b,c) Incorrect lattice and time step discretisation, where LBM simulates granular flows with constant viscosity $\nu \in [\nu_{\min}, \nu_{\max}]$.

$$\nu = \frac{t_r - 1/2}{3} \frac{\Delta S^2}{\Delta t}. \quad (22)$$

Inverting Eq. 22, and inserting Eq. 7, one obtains the constitutive law for the relaxation time:

$$t_r = \frac{1}{2} + 3 \frac{p\mu(I)}{\rho\dot{\gamma}} \frac{\Delta t}{\Delta S^2}. \quad (23)$$

It must be highlighted that stability and accuracy are maintained in LBM as long as t_r is within fixed limits. In agreement with the literature, these limits are set to $t_{r,\max} = 1.0$ and $t_{r,\min} = 0.5005$. LBM can, therefore, simulate only a specific range of viscosities:

$$\nu_{\min} = \frac{t_{r,\min} - 1/2}{3} \cdot \frac{\Delta S^2}{\Delta t}, \quad (24)$$

$$\nu_{\max} = \frac{t_{r,\max} - 1/2}{3} \cdot \frac{\Delta S^2}{\Delta t}. \quad (25)$$

Since the viscosity range is a function of ΔS and Δt , these parameters must be chosen correctly to simulate the correct range. To do this, it is necessary to compare ν_{\min} and ν_{\max} with an estimate of the viscosity of the flow to be simulated. Following a simple but effective approach, it is possible to obtain such an estimate by employing the analytical solution of the $\mu(I)$ rheology under simplified assumptions (Lagr ee et al., 2011). Under the hypothesis

of a steady-state flow of constant height h , on an inclined constant slope θ (Fig. 8), one obtains pressure p , velocity u , and viscosity ν as a function of depth z :

$$p(z) = \rho g h \left(1 - \frac{z}{h}\right) \cos \theta, \quad (26)$$

$$u(z) = \frac{2}{3} I_\theta \sqrt{g d \cos \theta} \frac{h^3}{d^3} \left[1 - \left(1 - \frac{z}{h}\right)^{3/2}\right], \quad (27)$$

$$\nu(z) = \frac{d \sin \theta \sqrt{g h}}{\sqrt{\cos \theta} I_\theta} \sqrt{1 - \frac{z}{h}}, \quad (28)$$

where I_θ is the inverse of the $\mu(I)$ function (Lagr ee et al., 2011).

Based on this simplified setup, Fig. 6 displays three different scenarios regarding the numerical and analytical viscosities as a function of the vertical coordinate $z \in [0, h]$. Fig. 6(a) shows the correct choice of time step Δt and lattice spacing ΔS . In this case, LBM can simulate the correct viscosity variation. Whereas Fig. 6(b) and 6(c) show setups where time step and lattice spacing are not chosen correctly. LBM applies a viscosity cut-off and simulates a reduced viscosity range whose upper/lower bounds are given by Eqs. 24 and 25.

3.4. Coupling between DA and 3D: Coupled model

As mentioned in the introduction, at the coupling section, the 3D model computes the velocity profile from the DA model variables, which are \bar{u} and h . However, the DA model is based on an unstructured triangular grid, while the 3D mesh is cubic (Figs. 2(b) and (d), respectively). Thus, it is necessary to project the DA variables to the 3D grid at the coupling section. Fig. 7 illustrates the logical procedure. The DA variables are based on mesh points (Fig. 7(a)) whose spacing is irregular in x and y directions (ΔS^* in Fig. 7(a)). Hence, the results are interpolated on a sequence of aligned points, whose spacing ΔS is equal to the 3D model mesh (Fig. 7(b)). Finally, the 3D velocity profile is computed (Fig. 7(c)) employing the analytical velocity profiles obtained on stationary conditions with the $\mu(I)$ rheology (Eq. 27). In order to convert a depth-averaged velocity into a 3D velocity profile, some assumptions are made. The $\mu(I)$ 3D velocity profile is adopted because, among others, this rheology has a convenient analytical solution for the velocity profile at steady-state. However, the flow could still be unsteady when impinging on a barrier. This aspect should be studied in future developments. Understanding how the profile can be altered to account for unsteady effects may be extremely helpful to improve the coupling algorithm.

The velocity profiles are rewritten as a function of \bar{u} , which can be obtained by integrating Eq. 27 along the flow depth:

$$\bar{u} = \frac{2}{5} I_\theta \frac{1}{d} \sqrt{g \cos \theta h^3}, \quad (29)$$

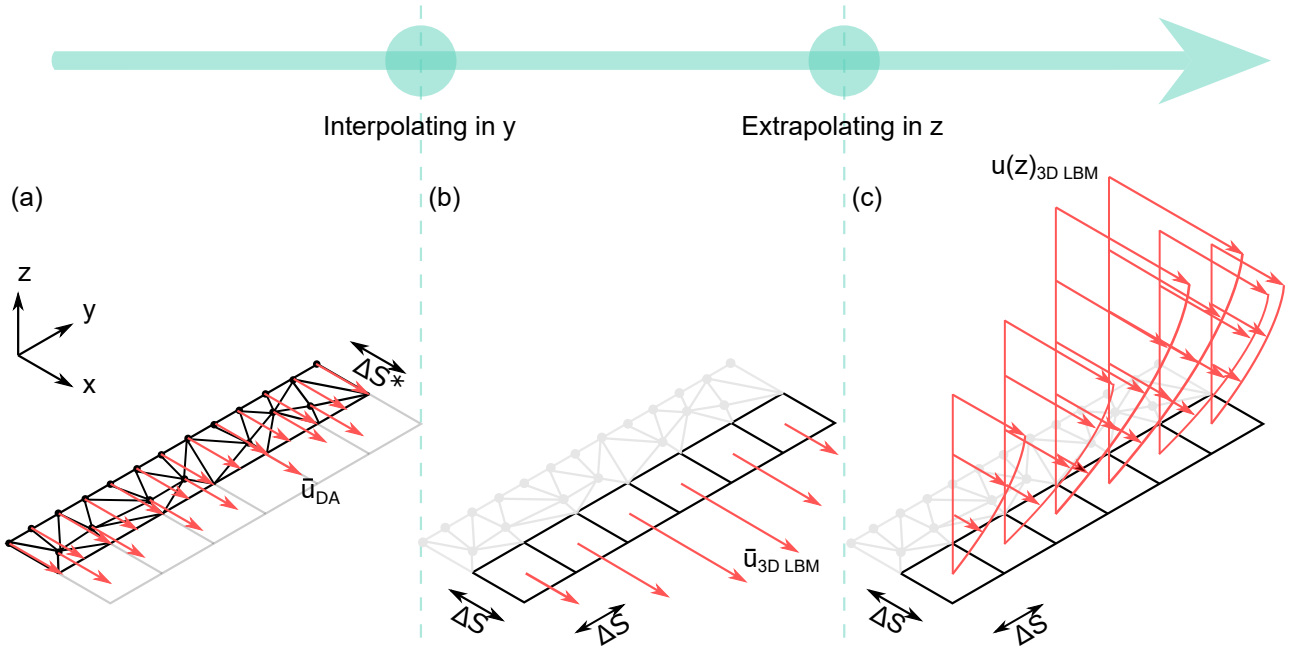


Figure 7: (a) DA results (flow height and depth-averaged velocity) on unstructured triangular (mesh Delaunay triangulation), (b) interpolated results on square mesh compatible with the 3D model mesh, (c) 3D velocity profile computed from DA on regular square mesh.

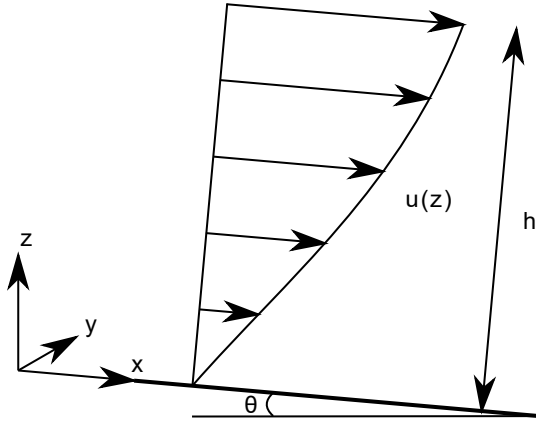


Figure 8: 1D flow down an inclined plane. Reference system, slope angle θ , analytical velocity profile $u(z)$, flow height h .

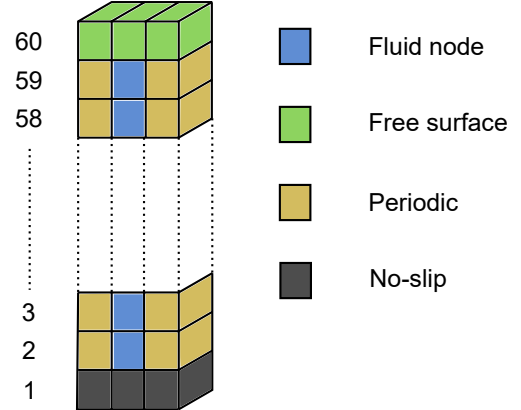


Figure 9: Boundary conditions and fluid area for 1D flow down an inclined plane.

by combining Eqs. 27 and 29 one obtains:

$$u(z, \bar{u}, h) = \frac{5}{3} \bar{u} \left[1 - \left(1 - \frac{z}{h} \right)^{3/2} \right], \quad (30)$$

which directly links the DA variables \bar{u} and h to the velocity along the height. This vertical velocity profile is then used as an inlet for the 3D model.

4. Numerical model validation: Frictional rheology and coupling

Since no implementation of frictional rheologies has been proposed for LBM, the 3D model of choice is benchmarked using the available analytical solutions (Lagrée et al.,

2011). A steady-state granular flow on an incline that extends indefinitely in the lateral directions x and y is studied. Two different setups are used: (i) a double-periodic, infinite flume, and (ii) an inlet-outlet configuration. The former validates the implementation of the $\mu(I)$ rheology, the latter the inlet condition. A uniform material is simulated with the same rheological parameters proposed by Jop et al. (2006): $\rho = 1500 \text{ kg/m}^3$, $d = 20 \text{ mm}$, base inertial number $I_0 = 0.279$, $\mu_s = 0.38$ and $\mu_d = 0.64$.

4.1. Double-periodic setup - validation of 3D frictional rheologies

This setup, first simulates a flow depth h and a slope angle θ fixed at 0.10 m and 25° , respectively. Figs. 8 and

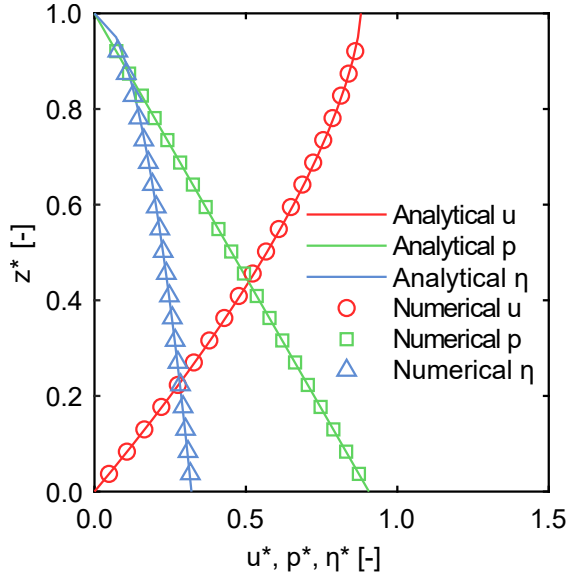


Figure 10: 1D flow down an inclined plane. Dimensionless velocity $u^* = u(z)/\sqrt{gh}$, pressure $p^* = p(z)/\rho gh$, and viscosity $\eta^* = \eta(z)/\sqrt{gh^3}$ along the vertical coordinate $z^* = z/h$. Comparison between 3D LBM and analytical solutions (Lagrée et al., 2011).

9 provide the graphical illustration of the lattice used and of the boundary conditions. An infinite flume is obtained by applying periodic boundary conditions along the x and y directions. Zero-velocity condition at the bottom of the flow, and zero-pressure at the free surface are imposed. The domain is discretised using a lattice with dimensions $1 \times 1 \times 60$ in the three directions. The time step Δt and lattice discretisation ΔS are $1 \cdot 10^{-4}$ s and $1.6 \cdot 10^{-3}$ m, respectively. The time step and the lattice discretisation are calibrated to simulate the correct range of viscosity (see Fig. 6(a)), and a regularisation factor $\lambda = 1.2 \cdot 10^{-4} \text{ s}^{-1}$ is applied.

Fig. 10 plots the comparison between the numerical results and the analytical solutions. For both setups, comparison of the values of pressure, viscosity, and velocity along the flow depth, and variation of the solution for a varying slope incline θ are made. The agreement with the analytical solution (Eqs. 26, 27, and 28) is excellent.

Using the same setup, the dependence of the maximum velocity (at the free surface, $z = h$) on the slope incline θ is also studied. To highlight the different behaviour of the $\mu(I)$ rheology with respect to more conventional rheologies, the profiles obtained with a Newtonian and a Bagnold formulation on the same problem (subscripts B and N, respectively) are also compared. For these rheologies, the velocity at the free surface is:

$$u_B(h) = \frac{2}{3} \sqrt{gd \sin \theta} \frac{h^3}{d^3}, \quad (31)$$

$$u_N(h) = \frac{2g \sin \theta h^2}{\nu}. \quad (32)$$

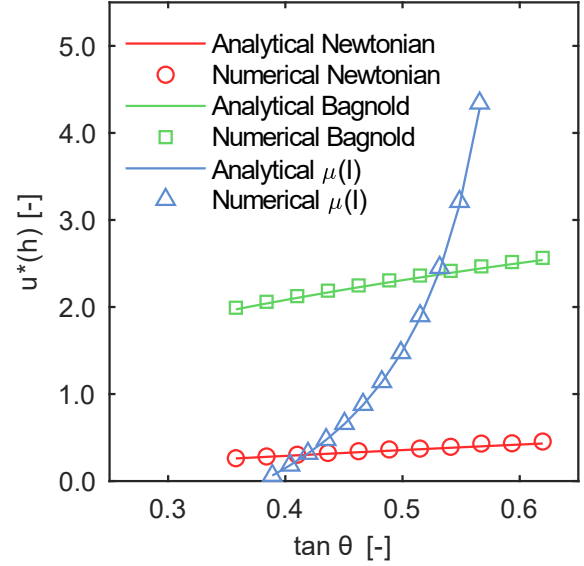


Figure 11: 1D flow down an inclined plane. Dimensionless velocity $u^*(h) = u(h)/\sqrt{gh}$ at the free surface with $\mu(I)$, Bagnold and Newtonian rheologies. Comparison between 3D LBM and analytical solutions.

The studied slope inclines in the range $\tan \theta \in [0.39, 0.56]$. With these parameters and boundary conditions, the $\mu(I)$ rheology yields steady-state flows. The lower bound is at the threshold of the no-flow condition μ_s .

Fig. 11 shows the numerical and analytical solutions of the velocity at the free surface as a function of $\tan \theta$. The fit with the analytical solution is excellent. The threshold for incipient motion is also captured correctly, with the flow progressively approaching the zero-velocity condition at $\tan \theta \rightarrow \mu_s$. Fig. 11 also illustrates how the flow conforms to the three states described by the $\mu(I)$ rheology. The are no flow for $\tan \theta < \mu_s$, steady-state dynamic equilibrium for $\mu_s \leq \tan \theta \leq \mu_d$, and velocity divergence for $\tan \theta > \mu_d$.

The Bagnold and Newtonian rheologies show a markedly different behaviour. Flow is always possible, even for the gentlest slopes, because no threshold stress for incipient motion is defined. Moreover, the velocity increases with $\tan \theta$, without diverging. All these aspects are in contrast with granular flows evidences, which proves the sensibility of the $\mu(I)$ rheology.

4.2. Finite-length domain: Validation of the inlet condition

The implementation of the inlet condition for the 3D LBM model and the $\mu(I)$ rheology is now benchmarked. To do this, the same analytical benchmark described in the previous section is employed: a steady-state flow on an infinite incline. However, the inlet benchmarking is done using a domain with fixed finite length $L = 100h$ (Fig. 12), and by applying an inlet condition at the upper boundary. Fig. 12 depicts the numerical scheme and the boundary conditions. The domain is discretised on a lattice with dimensions

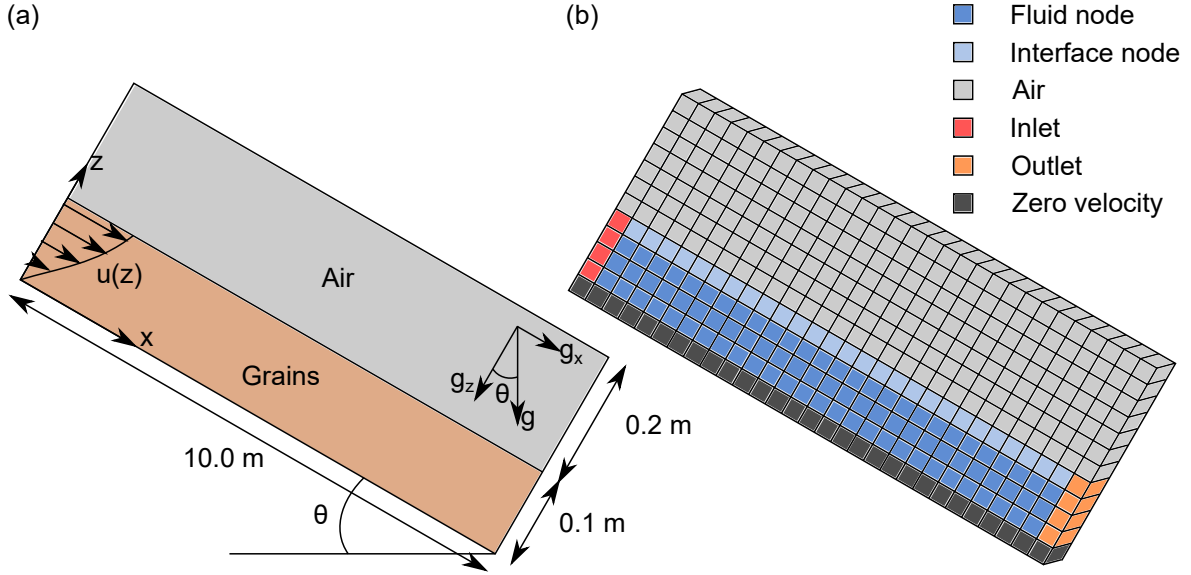


Figure 12: Finite-length channel with inlet condition: (a) domain and geometry, (b) boundary conditions and lattice configuration.

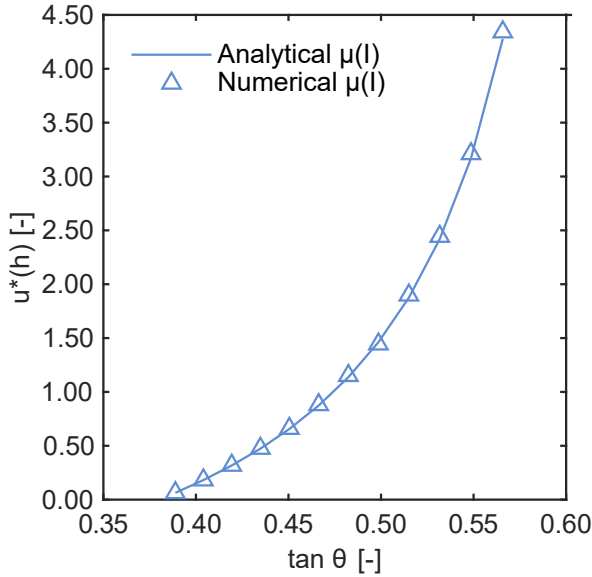


Figure 13: Finite-length channel with inlet condition. Dimensionless velocity at the free surface $u^*(h) = u(h)/\sqrt{gh}$ as a function of the slope incline.

$1000 \times 1 \times 30$ in x , y , and z , respectively. The lattice spacing $\Delta S = 1 \cdot 10^{-2}$ m guarantees enough points to accurately represent the flow. At $x = 0$ m, an inlet with constant mass flux ($h = 0.1$ m and $\bar{u} = 5.0$ m/s) is imposed. Hence, by employing the algorithm discussed in Section 3.4, the corresponding velocity profile is extrapolated, (see Fig. 12(a)). At $x = L$, an outlet condition is imposed.

Fig. 13 shows the numerical and analytical velocity at the free surface $u^*(h) = u(h)/\sqrt{gh}$ as a function of $\tan \theta$. An excellent agreement between numerical results

and analytical solutions (Eq. 27 (Lagrée et al., 2011)) is observed. It is possible to draw the same conclusions as Section 4 regarding the no-flow ($\tan \theta < \mu_s$), steady-state flow ($\mu_s < \tan \theta < \mu_d$), and unsteady flow ($\tan \theta > \mu_d$) conditions. Moreover, the inlet condition is tested with the $\mu(I)$ velocity profile condition (Eq. 30). Since the velocity results perfectly fit the analytical solutions, the implementation of the $\mu(I)$ rheology 3D inlet velocity profile proposed here is considered validated.

4.3. Regularisation

When changing the slope incline θ , a significant change in the velocity magnitude occurs, as predicted by Eq. 27. This corresponds to a change of the equivalent viscosity of the material, see Eq. 28. Thus, due to the viscosity cut-off discussed in Section 3.3, the simulation parameters must be adapted for each simulation in order to simulate the correct range of viscosity (see Fig. 6(a)). Since ΔS is fixed, in order to correctly discretise the flow, the time step must be adapted. The values of Δt which correspond to an optimised configuration are reported in Table 1.

The regularisation parameter λ must also be adapted, since it changes together with the timescale of the flow. It is possible to relate λ to the characteristic timescale of the flow T , which for this flow can be defined as:

$$T = \frac{h}{u(h)}, \quad (33)$$

where u can be obtained from the mean velocity predicted by Eq. 29.

Dimensional analysis suggests that the λ must be inversely proportional to T :

$$\lambda(T) = \frac{k}{T}, \quad (34)$$

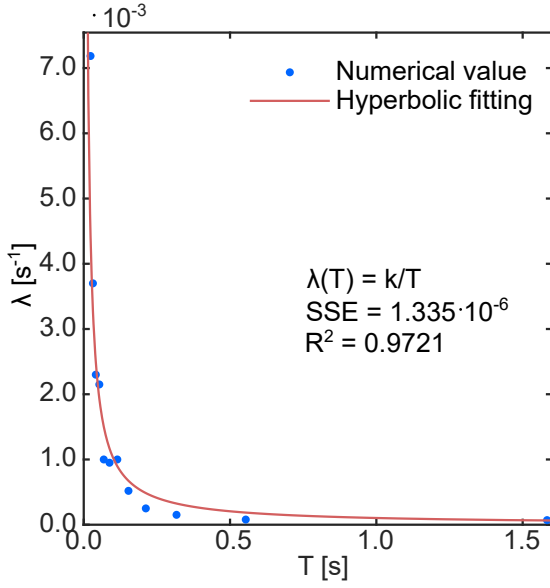


Figure 14: Calibration of the regularisation factor λ as a function of the flow timescale T .

Table 1

Validation of inlet condition. 3D LBM discretization and regularization.

ΔS [m]	Δt [s]	$\tan \theta$ [-]	λ [s ⁻¹]
1 · 10 ⁻²	4.4 · 10 ⁻⁵	0.389	4.0 · 10 ⁻⁶
	1.2 · 10 ⁻⁴	0.419	3.0 · 10 ⁻⁵
	2.0 · 10 ⁻⁴	0.435	9.8 · 10 ⁻⁵
	3.0 · 10 ⁻⁴	0.450	2.5 · 10 ⁻⁴
	4.0 · 10 ⁻⁴	0.466	5.2 · 10 ⁻⁴
	5.2 · 10 ⁻⁴	0.482	1.0 · 10 ⁻³
	4.0 · 10 ⁻⁴	0.499	1.0 · 10 ⁻³
	4.0 · 10 ⁻⁴	0.515	1.0 · 10 ⁻³
	4.0 · 10 ⁻⁴	0.532	2.2 · 10 ⁻³
	4.0 · 10 ⁻⁴	0.549	2.3 · 10 ⁻³
4.0 · 10 ⁻⁴	0.566	3.7 · 10 ⁻³	
4.0 · 10 ⁻⁴	0.583	7.2 · 10 ⁻³	

where k is a dimensionless parameter. No universal value has been proposed for this parameter, and thus it is determined empirically. Due to regularisation being widely employed, it might be beneficial to report the values used in this study. Stable solutions were found across the whole range of studied parameters by using $k = 1.1 \cdot 10^{-4}$. Fig. 14 shows how k was obtained by fitting the simulation parameters with a hyperbola.

5. Application of multi-domain framework to a laboratory flow

In this final section, the coupled DA-3D model is validated, and thus the coupling algorithm proposed in Section 3.4. The coupled model ultimately targets the simulation of real debris-flow channels. This is the geometry where it is most advantageous, because obstacles or barriers are usually located only on a limited portion of the basin.

However, data from in-situ measurements is notoriously difficult to interpret. Obtaining reliable and coherent data from sites is an active area of research (Leonardi and Pirulli, 2020). Therefore, a site geometry would not be optimal for benchmarking purposes.

It was opted to validate the coupled model on a simpler, more controlled environment as a first application. A replica of the laboratory experiment conducted by Moriguchi et al. (2009) is carried out. Moriguchi et al. (2009) assembled the flume illustrated in Fig. 15(a). The flume can be considered a model of a channel with a mitigation structure at its bottom. The experiments were conducted with dry fine Toyoura sand. The sand was fairly uniform, with mean particle size d of 0.2 mm. To allow observation, one side of the flume was built in acrylic. The flume length and width were 2.5 m and 0.3 m, respectively, while its slope angle θ was 45°. In the original paper, Moriguchi et al. (2009) carried out experiments with angles steeper than 45°. However, since no result regarding the free surface configuration is shown in their paper, numerical analyses with θ steeper than 45° are not run.

To carry out their studies, a container filled with sand was placed at the flume top. The container had a gate which could be opened quickly to initiate the flow. A barrier was placed at the flume bottom. Fig. 15 shows the assembled flume for the experiment and its numerical sketch. The experiment was recorded, and had an overall duration of approximately 1.6 s. The interested reader can find more details in the original paper (Moriguchi et al., 2009).

These experiments are particularly suitable to validate the proposed numerical model, since observations are very accurate. Moreover, the tested material is mono-dispersed, and dry. Thus, the underlying hypotheses of the $\mu(I)$ rheology are satisfied.

It is important to understand that analyses with mono-disperse dry sand are carried out. Essentially, there are essentially two reasons for this choice. (i) Moriguchi et al. (2009) studied mono-disperse dry Toyoura sand. Since the validation of the coupled model was based on back analysis of this dry mono-disperse sand, other experiments would be needed in order to validate a bi-disperse or saturated model. (ii) More importantly, non-uniform flows cause segregation. However, only DA models have been validated for problems involving segregation (Iverson and Denlinger, 2001; Gray and Ancey, 2011; Barker et al., 2021), whereas for 3D models there is no consensus on how this could be achieved.

To cross-validate the model, the flow is replicated with a pure 3D LBM model, with a pure DA model, and finally with the coupled model. It is then possible to compare the performances of the three approaches and draw some preliminary considerations. For consistency, the DA and the 3D models should implement equivalent rheological parameters. To do so, the following procedure is adopted. Firstly, the 3D model is calibrated. It is sensible to use the 3D model to study the flow, mainly because the obstacle imposes a vertical component of the flow which only a 3D model can accurately compute. Moreover, the flow-structure

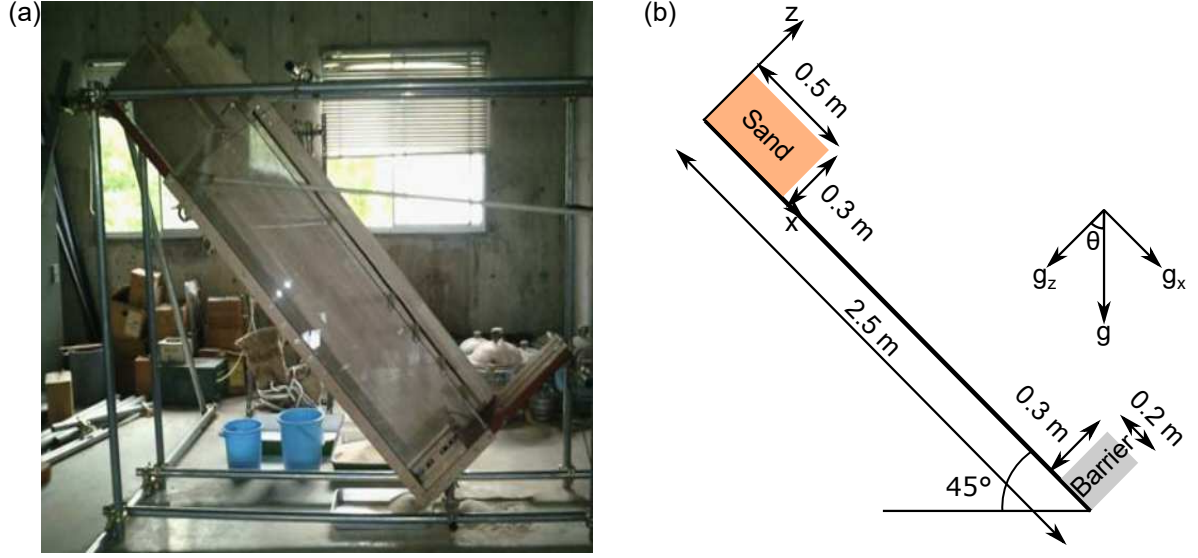


Figure 15: (a) Laboratory flume assembled by Moriguchi et al. (2009). (b) Sketch for numerical simulations. A container filled with sand is placed at the top of the flume, at its bottom a rigid barrier. The flume inclination is $\theta = 45^\circ$.

Table 2

Depth-averaged and local $\mu(I)$ rheological parameters.

Depth-averaged $\mu(I)$		Local $\mu(I)$		
μ_s	[-]	0.3249	μ_s [-]	0.3249
μ_d	[-]	0.7002	μ_d [-]	0.7002
β	[-]	0.75	I_0 [-]	0.3227
L	[-]	7.5	ρ_p [kg/m^3]	2600
d	[mm]	0.2	d [mm]	0.2

interaction is a complex problem with a large number of details i.e. granular jump, reflected wave, dead zone, and airborne jet. These details can be studied with a good degree of approximation, from a 3D model. In the 3D LBM model, time and space are discretised as follows: $\Delta t = 1 \cdot 10^{-5}$ s and $\Delta S = 5 \cdot 10^{-3}$ m. With this discretisation, LBM can simulate the expected viscosity range (Fig. 6(a)). Starting from this, the parameters of the depth-averaged $\mu(I)$ rheology are calculated, i.e. μ_s , μ_d , β , L , and d . However, μ_s and μ_d are identical in both versions of the rheology, and d is a known material parameter. β is known from similar studies (Pouliquen and Forterre, 2002; GDR MiDi, 2004). Finally L is computed by inverting Eq. 6 with $\Phi = 0.6$ (Jop, 2015). All parameters are collected in Table 2. Note that the local parameters are in agreement with similar studies (Lagrée et al., 2011; Gesenhues et al., 2019). The coupled model is discussed in detail in Section 5.3.

For the back-analysis of the experiments, two variables are reported: free surface evolution with its final configuration and flow velocity contours. Figs. 16 and 17 show, in four different time frames (0.4 s, 0.8 s, 1.2 s, 1.6 s) the free surface shape and the velocity contours. These time frames are shown since they are the ones reported in the work of Moriguchi et al. (2009).

5.1. Back-analysis of the flow: 3D LBM

As shown in Fig. 16 the results of the 3D model are very close to the experimental observations. This match is expected due to the high accuracy of the 3D model, with all phases of the phenomenon (triggering, transportation, and deposition) faithfully reproduced. At 0.4 s it is particularly evident how both the results of the 3D model match the experimental results at the rear and at the front. This is proof that the 3D model is able to accurately reproduce the collapse of an unstable mass and its following transportation phase, at least in these idealised conditions. Furthermore, at the 1.6 s, for $x > 2.3$ m (ahead of the barrier position), the free surface shows a non-constant slope. This is caused by the barrier, whose volume influences the depositional process of the flow. This is a clear indication of how the 3D model can accurately reproduce the presence of obstacles.

Regarding Fig. 17, no direct measurement of the velocity is available from the experiments. Nevertheless, there is a unique match between the velocity and the mass position during the realisations. Since in Fig. 16 the 3D model correctly predicts the mass position, the velocity shown in Fig. 17 must be approximately the same as the one developed in the flume. Thus, the conclusion may be that the actual velocity that occurred in the flume is similar to the velocity computed in the 3D model.

5.2. Back-analysis of the flow: depth-averaged model

Table 2 shows the rheological parameters employed in the DA model. Although the parameters are equivalent to those used for the 3D model, the numerical results do not equally match the experimental series. In particular, in Fig. 16 one can see how the DA predicts an offset compared to the experimental recordings. Even at 0.4 s, the front

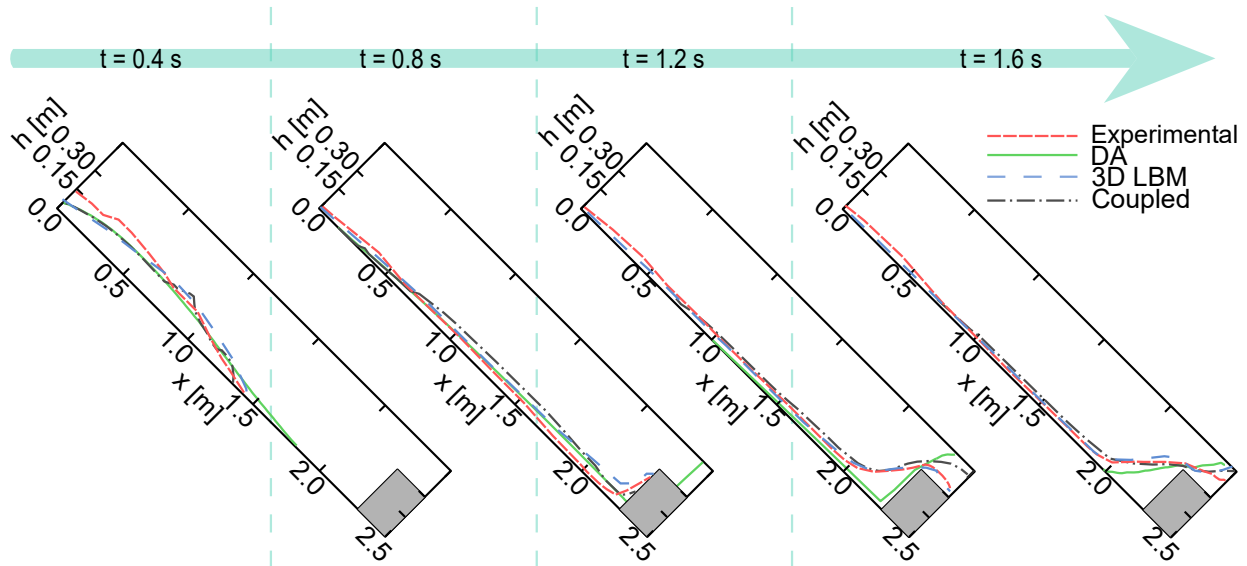


Figure 16: 3D flow of granular material over inclined plane. The four representations plot the free surface configuration at different time. From left to right: 0.4 s, 0.8 s, 1.2 s, 1.6 s.

position is ahead of the experimental results. The causes of this over-prediction are to be found in the limits of the DA models (see Section 3.2). Although at 0.4 s the flow adheres to the shallowness assumption ($h/\ell \ll 1$), the inaccuracy is a consequence of what occurred in the earlier time steps. At triggering, the shallowness assumption is not met because $h = 0.3$ m and $\ell = 0.5$ m, leading to $h/\ell = 0.6$. Thus, in the first time steps, the DA model neglects the vertical momentum even in areas where this is not appropriate. As long as the flow path is long enough, this error is compensated in the runout phase. But in this study the flow path is too short to compensate for this error. Alternatively, a higher μ_s could have been employed to reduce the initial velocity overestimation. However, in this study, the best-fit friction angle would be of the order of 0.9. Such a high value of μ_s is unphysical and would lead to unrealistic results in the 3D model. Furthermore, when the flow reaches the flume bottom (between 0.8 s and 1.2 s), the shape of the free surface appears unphysical. In particular, it seems like the flow is not influenced by the barrier at all. Moreover, when the flow front reaches the obstacle, a vertical jet develops. Vertical jets occur when granular flows at high Froude numbers impinge on obstacles. Such a jet cannot be accurately replicated in the simulation carried out in this paper due to the numerical scheme employed in the DA model of choice, due to a classic finite-difference scheme. To accurately resolve vertical jets, more complex numerical tools are required (see Section 3.1). Finally, at 1.6 s the flow stops, and the slope of the free surface has the same value as the frictional angle. Once more, this result cannot be accepted because the influence of the barrier is neglected. There are two possible explanations for these inaccuracies. First, the shallowness condition ($h/L \ll 1$) is not met everywhere in the domain, and especially at flow initiation. Moreover, special attention should be paid to the

integration scheme. Since the DA model of choice does not implement a high-resolution non-oscillatory scheme, shock waves and granular jumps cannot be computed accurately (Gray et al., 2003; Wang et al., 2004; Pudasaini et al., 2005). Hence, the flow-structure interaction is over-simplified, and the results at impact are inaccurate.

Fig. 17 retraces the same inaccuracies as Fig. 16. The same conclusions mentioned above can be proposed as possible explanations for the numerical inaccuracies.

5.3. Back-analysis of the flow: coupled model

In this final section, the results obtained using the coupled model are discussed. In order to couple the DA and the 3D model, it is necessary to define the position of a coupling-section, which splits the domains into two sub-domains and applies the algorithm discussed in Section 3.4. It is important to highlight that this study does not aim to find the optimal position of the coupling section, which, in general, is a problem related to the necessity to minimise computational resources. Rather, the aim is to demonstrate that coupling a DA and a 3D model is feasible and convenient.

For the current benchmark, the setup for the coupled model is graphically detailed in Fig. 18. At 0.7 m, the coupling section separates the domain into two parts in agreement with the strategy described in Section 3.4. The DA model solves the upper part of the computational domain, and the 3D LBM solver operates on the lower part, which contains the obstacle. The position of 0.7 m is chosen since at this location the condition $h/L \ll 1$ is reasonably met. Thus, the DA results are reliable.

The results in Fig. 16 support the application of the coupled model. Despite the inaccuracies of the DA model, once the 3D model converts the depth-averaged velocity into a velocity profile, experimental observations are matched. Moreover, the runup and the depositional process are similar

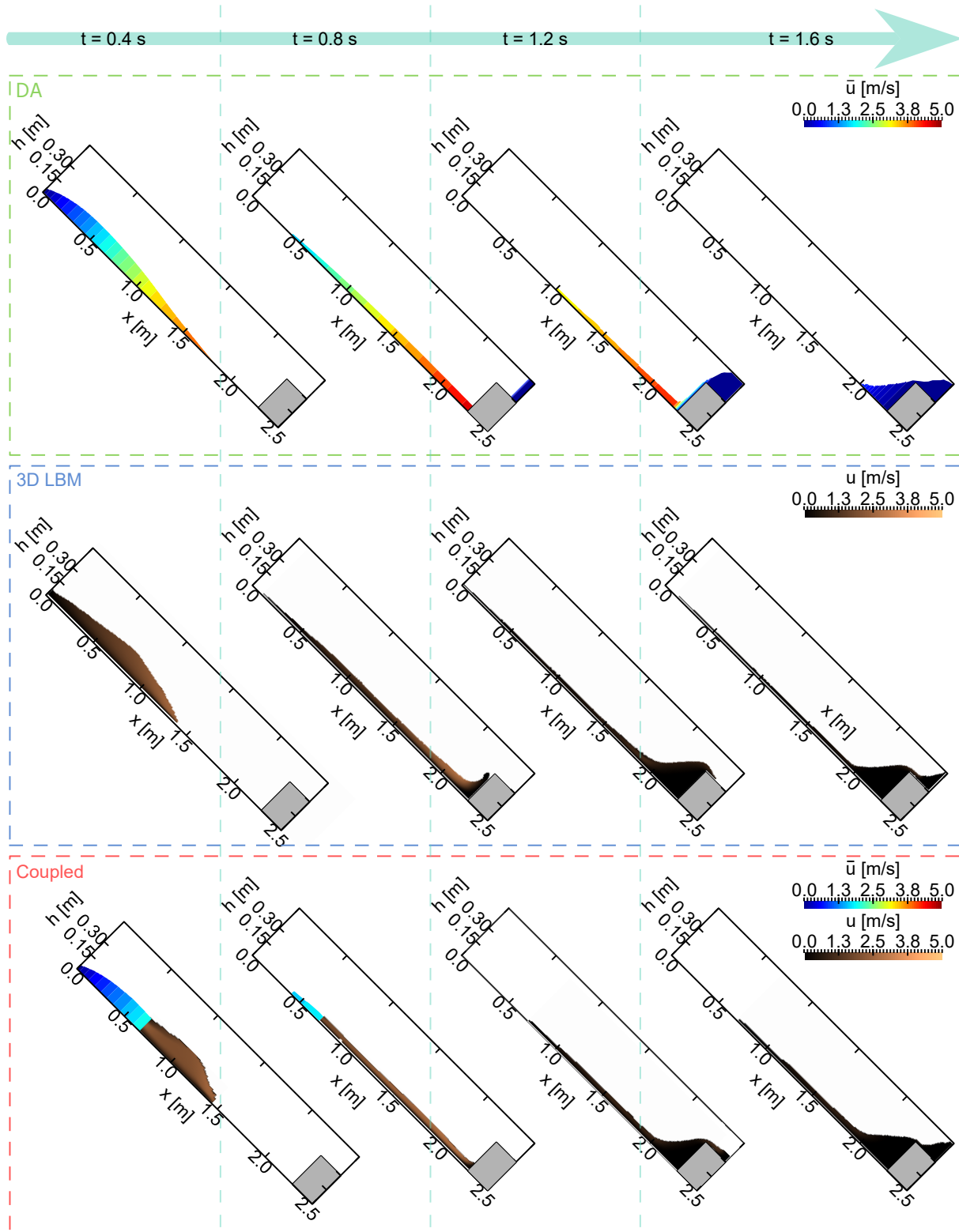


Figure 17: Flow velocity for the tested models. Each row represents a numerical model results at a different time. Downwards: DA, 3D, and coupled, from left to right: 0.4 s, 0.8 s, 1.2 s, 1.6 s.

to the pure 3D LBM model and to the experimental results. At 1.6 s, the shape of the free surface is influenced by the presence of the barrier. The numerical results (both 3D and coupled) are very similar to the experimental results. The

differences are in the order of a few centimetres, and can be considered negligible. Indeed, both the 3D model and coupled model are able to replicate the flow with remarkable accuracy. These results suggest that the limitations of the DA

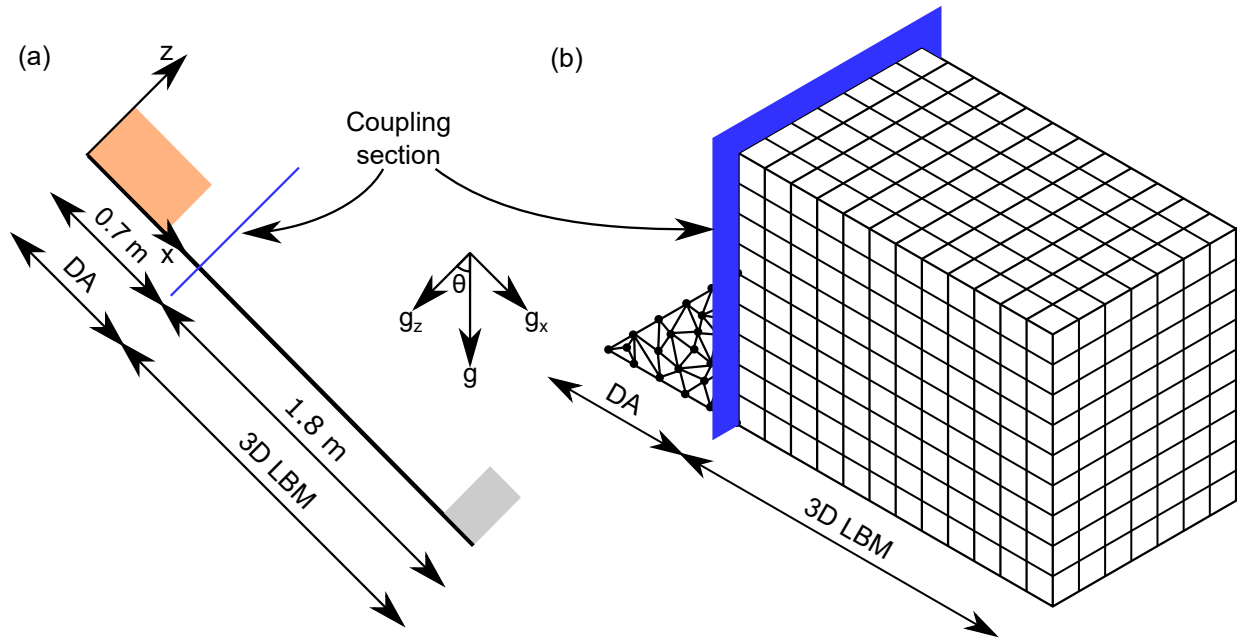


Figure 18: 3D flow of granular material over inclined plane. (a) Numeric scheme and geometry. (b) DA and 3D meshes (unstructured and regular respectively).

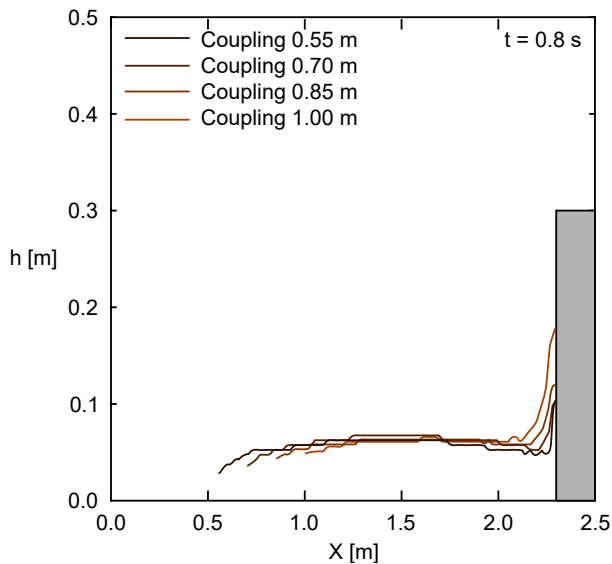


Figure 19: Free surface configuration at 0.8s for coupling section at 0.55m, 0.70m, 0.85m, and 1.00m.

model can be recovered by the 3D model, thus substantiating the capabilities of the DA-3D coupling.

Fig. 17 shows the flow velocity. As described in Section 5.1, since there is a correspondence between time and the mass position (Fig. 16), the velocity in Fig. 17 corresponds to the one observed in the flume.

5.4. Preliminary considerations on the coupling section location and the computing efficiency

Some preliminary comments on the location of the coupling section and computational efficiency can be made. A

set of simulations to show the effect of a change in the location of the coupling section are performed. While there is a certain degree of freedom in choosing the location of the coupling section, this should not be too close to where impact takes place, or to the initial column collapse. In these areas, the flow shows a non-negligible vertical momentum, which makes the coupling unsuitable. Hence, a theoretically consistent location of the coupling section should in this case be in the range $x = [0.55 \text{ m}, 1 \text{ m}]$. Fig. 19 shows the results of simulations with the coupling section at 0.55 m, 0.70 m, 0.85 m, and 1.00 m. Free-surface configurations for these setups are taken at 0.8 s and the results, albeit exhibiting slight differences, are comparable. The differences may be caused by the assumption of steady-state, which introduces an error, since the flow may still be accelerating at the coupling position.

Some preliminary observation regarding computational efficiency, can be discussed. The coupling between DA and 3D models is ultimately aimed at improving the computational efficiency of a 3D approach, making the simulation of natural channels more achievable. In the proposed validation this is not visible, since 3D domain constitutes a large portion of the overall domain in any case. If, on the other hand, we were to simulate a natural channel, the overall size of the domain would be a few orders of magnitude larger than the domain in which the 3D model is required (the area around the obstacle). Thus, the coupled model has the potential of reducing computational times exponentially.

6. Conclusions

In this work, a DA-3D coupled model to study granular flows has been proposed. Coupling a DA and a 3D model

is convenient because DA does not represent flow-structure interaction well if vertical acceleration is not taken into account, unless a sophisticated numerical integration scheme is employed. Furthermore, 3D models do not add relevant information if no structure is present in the path of the flows. Thus, splitting the domain into two parts can optimise the computational time without losing relevant information due to the vertical integration.

3D LBM was implemented because it offers distinct advantages if compared to more traditional fluid solvers. The main advantage of LBM is that parallelisation is easy to achieve. Moreover, DEM can easily be combined with LBM to simulate bi-dispersed flows in free-surface conditions, even in complex geometries. A non-uniform sand with water was not considered, although in nature this would be a common situation. It was preferable to focus on a dry uniform material sand because non-uniform granular flows imply segregation. In the literature, several DA models able to consider segregation have been proposed, such as in Iverson and Denlinger (2001); Gray and Ancey (2011); Barker et al. (2021). However, equivalent formulations, to the best of our knowledge, have not yet been implemented in 3D models.

The implementation of the $\mu(I)$ rheology in a 3D LBM code was validated first. A 1D flow over an infinitely extended inclined plane and a 2D channel with constant inlet conditions were studied. The numerical results fit the analytical solutions (Lagrée et al., 2011) very well.

Most importantly, the coupling between a DA and a 3D model was tested at the laboratory scale. Numerical analyses to replicate the study conducted by Moriguchi et al. (2009) with the DA, the 3D LBM and the coupled model were carried out. In the coupled model, as long as the flow did not approach a barrier, DA was employed to solve the flow motion. When the flow crossed a coupling section, the 3D model carried out the remaining part of the analysis. This second part of the analysis included the flow-structure interaction. The results are encouraging, since not only did the 3D model successfully replicate the experiment, but the coupled model was able to satisfactorily compute the flow motion as well.

This work has produced some encouraging results in terms of coupling DA and 3D models. However, since the model was validated at the laboratory scale, no large-scale effects could be observed, while the material employed was fairly uniform sand. It would be interesting to repeat the numerical analyses using large-scale facilities, as in this context the material would not be uniform sand but a mud-debris mixture with non-uniform granulometry. Non-uniform material and large-scale geometry would allow more rigorous testing of a coupled model with all its features, i.e. the position of the coupling section, the coupling algorithm, and the coupling rheological parameters.

Acknowledgements

We gratefully acknowledge the support of Prof. Moriguchi. The videos regarding the experiments conducted by him and

his team enabled us to calibrate the models discussed in this paper. This study was made possible thanks to funding from the “Call for proposal - Joint research projects with top universities” in the frame of the General Agreement 2016-2018 signed between Politecnico di Torino and the Compagnia di San Paolo. The Computational resources were provided by HPC@POLITO, a project of Academic Computing within the Department of Control and Computer Engineering at Politecnico di Torino (<http://www.hpc.polito.it>)

References

- Adhianto, L., Banerjee, S., Fagan, M., Krentel, M., Marin, G., Mellor-Crummey, J., Tallent, N.R., 2010. HPCTOOLKIT: Tools for performance analysis of optimized parallel programs. *Concurrency Computation Practice and Experience* 22, 685–701. doi:10.1002/cpe.
- Arkeryd, L., 1972. On the Stationary Boltzmann Equation in R^n . *International Mathematics Research Notices* 2000, 624–641.
- Barker, T., Rauter, M., Maguire, E.S., Johnson, C.G., Gray, J.M., 2021. Coupling rheology and segregation in granular flows. *J. Fluid Mech.* 909. doi:10.1017/jfm.2020.973.
- Barker, T., Schaeffer, D.G., Bohorquez, P., Gray, J.M., 2015. Well-posed and ill-posed behaviour of the μ -rheology for granular flow. *Journal of Fluid Mechanics* 779, 794–818. doi:10.1017/jfm.2015.412.
- Bhatnagar, P.L., Gross, E.P., Krook, M., 1954. A Model for Collision Processes in Gases. I. Small Amplitude Processes in Charged and Neutral One-Component Systems. *Phys. Rev.* 94, 511–525. URL: <https://link.aps.org/doi/10.1103/PhysRev.94.511>, doi:10.1103/PhysRev.94.511.
- Canelli, L., Ferrero, A.M., Migliazza, M., Segalini, A., 2012. Debris flow risk mitigation by the means of rigid and flexible barriers - Experimental tests and impact analysis. *Natural Hazards and Earth System Science* 12, 1693–1699. doi:10.5194/nhess-12-1693-2012.
- Cercignani C., 1988. *The Boltzmann Equation and Its Applications*. volume 67. 1 ed., Springer, New York, NY. doi:<https://doi.org/10.1007/978-1-4612-1039-9>.
- Chialvo, S., Sun, J., Sundaresan, S., 2012. Bridging the rheology of granular flows in three regimes. *Physical Review E - Statistical, Nonlinear, and Soft Matter Physics* 85, 1–8. doi:10.1103/PhysRevE.85.021305, arXiv:1201.5862.
- Chien-Yuan, C., Tien-Chien, C., Fan-Chieh, Y., Wen-Hui, Y., Chun-Chieh, T., 2005. Rainfall duration and debris-flow initiated studies for real-time monitoring. *Environmental Geology* 47, 715–724. doi:10.1007/s00254-004-1203-0.
- Chiou, M.C., Wang, Y., Hutter, K., 2005. Influence of obstacles on rapid granular flows. *Acta Mechanica* 175, 105–122. doi:10.1007/s00707-004-0208-9.
- Choi, S.K., Lee, J.M., Kwon, T.H., 2018. Effect of slit-type barrier on characteristics of water-dominant debris flows: small-scale physical modeling. *Landslides* 15, 111–122. doi:10.1007/s10346-017-0853-4.
- Cleary, P.W., Sawley, M.L., 2002. DEM modelling of industrial granular flows: 3D case studies and the effect of particle shape on hopper discharge. *Applied Mathematical Modelling* 26, 89–111. doi:10.1016/S0307-904X(01)00050-6.
- Coussot, P., Meunier, M., 1996. Recognition, classification and mechanical description of debris flows. *Earth-Science Reviews* 40, 209–227. doi:10.1016/0012-8252(95)00065-8.
- Desplat, J.C., Pagonabarraga, I., Bladon, P., 2001. Ludwig: A parallel Lattice-Boltzmann code for complex fluids. *Computer Physics Communications* 134, 273–290. doi:10.1016/S0010-4655(00)00205-8, arXiv:0005213.
- Douady, S., Andreotti, B., Daerr, A., 1999. On granular surface flow equations. *European Physical Journal B* 11, 131–142. doi:10.1007/BF03219163.
- Dunatunga, S., Kamrin, K., 2015. Continuum modelling and simulation of granular flows through their many phases. *Journal of Fluid Mechanics* 779, 483–513. doi:10.1017/jfm.2015.383, arXiv:1411.5447.

- Franci, A., Cremonesi, M., 2019. 3D regularized $\mu(I)$ -rheology for granular flows simulation. *Journal of Computational Physics* 378, 257–277. URL: <https://doi.org/10.1016/j.jcp.2018.11.011>, doi:10.1016/j.jcp.2018.11.011.
- García-Delgado, H., Machuca, S., Medina, E., 2019. Dynamic and geomorphic characterizations of the Mocoa debris flow (March 31, 2017, Putumayo Department, southern Colombia). *Landslides* 16, 597–609. doi:10.1007/s10346-018-01121-3.
- GDR MiDi, 2004. On dense granular flows. *The European physical journal. E, Soft matter* 14, 341–365. doi:10.1140/epje/i2003-10153-0.
- Gesenhues, L., Camata, J.J., Côrtes, A.M., Rochinha, F.A., Coutinho, A.L., 2019. Finite element simulation of complex dense granular flows using a well-posed regularization of the $\mu(I)$ -rheology. *Comput. Fluids* 188, 102–113. URL: <https://doi.org/10.1016/j.compfluid.2019.05.012>, doi:10.1016/j.compfluid.2019.05.012.
- Gray, J.M., Ancey, C., 2011. Multi-component particle-size segregation in shallow granular avalanches. *J. Fluid Mech.* 678, 535–588. doi:10.1017/jfm.2011.138.
- Gray, J.M., Edwards, A.N., 2014. A depth-averaged $\mu(I)$ -rheology for shallow granular free-surface flows. *Journal of Fluid Mechanics* 755, 503–534. doi:10.1017/jfm.2014.450.
- Gray, J.M., Tai, Y.C., Noelle, S., 2003. Shock waves, dead zones and particle-free regions in rapid granular free-surface flows. *Journal of Fluid Mechanics* 491, 161–181. doi:10.1017/S0022112003005317.
- Harting, J., Chin, J., Venturoli, M., Coveney, P.V., 2005. Large-scale lattice Boltzmann simulations of complex fluids: Advances through the advent of computational Grids. *Philosophical Transactions of the Royal Society A: Mathematical, Physical and Engineering Sciences* 363, 1895–1915. doi:10.1098/rsta.2005.1618, arXiv:0501021.
- He, X., Chen, S., Zhang, R., 1999. A Lattice Boltzmann Scheme for Incompressible Multiphase Flow and Its Application in Simulation of Rayleigh-Taylor Instability. *Journal of Computational Physics* 152, 642–663. doi:10.1006/jcph.1999.6257.
- He, X., Luo, L.S., 1997. Theory of the lattice Boltzmann method: From the Boltzmann equation to the lattice Boltzmann equation. *PHYSICAL REVIEW E* 56, 6811–6817. doi:10.1103/PhysRevE.56.6811.
- Hürlimann, M., Rickenmann, D., Graf, C., 2003. Field and monitoring data of debris-flow events in the Swiss Alps. *Canadian Geotechnical Journal* 40, 161–175. doi:10.1139/t02-087.
- Hutter, K., Koch, T., Plüüss, C., Savage, S.B., 1995. The dynamics of avalanches of granular materials from initiation to runout. Part II. Experiments. *Acta Mechanica* 109, 127–165. doi:10.1007/BF01176820.
- Iverson, R.M., 2003. The debris-flow rheology myth. *International Conference on Debris-Flow Hazards Mitigation: Mechanics, Prediction, and Assessment, Proceedings 1*, 303–314.
- Iverson, R.M., 2015. Scaling and design of landslide and debris-flow experiments. *Geomorphology* 244, 9–20. URL: <http://dx.doi.org/10.1016/j.geomorph.2015.02.033>, doi:10.1016/j.geomorph.2015.02.033.
- Iverson, R.M., Denlinger, R.P., 2001. Flow of variably fluidized granular masses across three-dimensional terrain. *Journal of Geophysical Research* 106, 537–552.
- Jenkins, J.T., Askari, E., 1999. Hydraulic theory for a debris flow supported on a collisional shear layer. *Chaos* 9, 654–658. doi:10.1063/1.166439.
- Jop, P., 2015. Rheological properties of dense granular flows. *Comptes Rendus Physique* 16, 62–72. URL: <http://dx.doi.org/10.1016/j.crhy.2014.12.001>, doi:10.1016/j.crhy.2014.12.001, arXiv:1503.05452.
- Jop, P., Forterre, Y., Pouliquen, O., 2005. Crucial role of sidewalls in granular surface flows: Consequences for the rheology. *Journal of Fluid Mechanics* 541, 167–192. doi:10.1017/S0022112005005987, arXiv:0503425.
- Jop, P., Forterre, Y., Pouliquen, O., 2006. A constitutive law for dense granular flows. *Nature* 441, 727–30. doi:10.1038/nature04801.
- Kandhai, D., Koppern, A., Hoekstra, A.G., Kataja, M., Timonen, J., Slood, P.M., 1998. Lattice-Boltzmann hydrodynamics on parallel systems. *Computer Physics Communications* 111, 14–26. doi:10.1016/s0010-4655(98)00025-3.
- Kazemian, Y., Esfahani, J.A., Rashidi, S., 2018. Enhancing the convergence speed of numerical solution using the flow rate control in a novel lattice Boltzmann method. *European Physical Journal Plus* 133. doi:10.1140/epjp/i2018-12373-6.
- Kilburn, R.J., 1998. and of Fragment Dynamics. *Transport* 103.
- Körner, C., Thies, M., Hofmann, T., Thürey, N., Råde, U., 2005. Lattice Boltzmann model for free surface flow for modeling foaming. *Journal of Statistical Physics* 121, 179–196. doi:10.1007/s10955-005-8879-8.
- Lagrée, P.Y., Staron, L., Popinet, S., 2011. The granular column collapse as a continuum: Validity of a two-dimensional Navier-Stokes model with a $\mu(I)$ -rheology. *Journal of Fluid Mechanics* 686, 378–408. doi:10.1017/jfm.2011.335.
- Larsen, M., Wieczorek, G., Eaton, L., Torres-Sierra, H., 2001. Natural Hazards on Aluvial Fans: The Debris Flow and Flash flood disaster of December 1999, Vargas State, Venezuela THE DEBRIS FLOW AND FLASH FLOOD DISASTER OF DECEMBER 1999, VARGAS STATE, VENEZUELA. *Proceedings of the Sixth Caribbean Islands Water Resources Congress 00965*, 1–7. URL: <http://www.stri.si.edu/sites/publications/PDFs/Larsen-et-al-Venez-6Carib-2001.pdf>.
- Leonardi, A., Pirulli, M., 2020. Analysis of the load exerted by debris flows on filter barriers: Comparison between numerical results and field measurements. *Computers and Geotechnics* 118, 103311. doi:10.1016/j.compgeo.2019.103311.
- Leonardi, A., Pirulli, M., Barbero, M., Barpi, F., Borri-Brunetto, M., Pallara, O., Scavia, C., Segor, V., 2021. Impact of Debris Flows on Filter Barriers: Analysis Based on Site Monitoring Data. *Environmental & Engineering Geoscience* 27, 195–212. URL: <https://doi.org/10.2113/EEG-D-20-00013>, doi:10.2113/EEG-D-20-00013, arXiv:https://pubs.geoscienceworld.org/aeg/eeg/article-pdf/27/2/195/5298822/i1078-
- Leonardi, A., Wittel, F.K., Mendoza, M., Vetter, R., Herrmann, H.J., 2016. Particle-Fluid-Structure Interaction for Debris Flow Impact on Flexible Barriers. *Computer-Aided Civil and Infrastructure Engineering* 31, 323–333. doi:10.1111/mice.12165, arXiv:1409.8034.
- Li, X., Zhao, J., 2018. A unified CFD-DEM approach for modeling of debris flow impacts on flexible barriers. *International Journal for Numerical and Analytical Methods in Geomechanics* 42, 1643–1670. doi:10.1002/nag.2806.
- Major, J.J., 1997. Depositional processes in large-scale debris-flow experiments. *Journal of Geology* 105, 345–366. doi:10.1086/515930.
- Mangeney-Castelnau, A., 2003. Numerical modeling of avalanches based on Saint Venant equations using a kinetic scheme. *Journal of Geophysical Research* 108, 1–18. doi:10.1029/2002jb002024.
- Marchi, L., Arattano, M., Deganutti, A.M., 2002. Ten years of debris-flow monitoring in the Moscardo Torrent (Italian Alps). *Geomorphology* 46, 1–17. doi:10.1016/S0169-555X(01)00162-3.
- Mazzeo, M.D., Coveney, P.V., 2008. HemeLB: A high performance parallel lattice-Boltzmann code for large scale fluid flow in complex geometries. *Computer Physics Communications* 178, 894–914. doi:10.1016/j.cpc.2008.02.013.
- McCracken, M.E., Abraham, J., 2005. Multiple-relaxation-time lattice-Boltzmann model for multiphase flow. *Physical Review E - Statistical, Nonlinear, and Soft Matter Physics* 71. doi:10.1103/PhysRevE.71.036701.
- Mohamad, A., 2011. *Lattice Boltzmann Method: Fundamentals and Engineering Applications with Computer Codes*. Springer. doi:10.1007/978-0-85729-455-5.
- Moriguchi, S., Borja, R.I., Yashima, A., Sawada, K., 2009. Estimating the impact force generated by granular flow on a rigid obstruction. *Acta Geotechnica* 4, 57–71. doi:10.1007/s11440-009-0084-5.
- Naef, D., Rickenmann, D., Rutschmann, P., W McArdell, B., 2006. Comparison of flow resistance relations for debris flows using a one-dimensional finite element simulation model. *Natural Hazards and Earth System Sciences* 6, 155–165. doi:10.5194/nhess-6-155-2006.
- Nikolopoulos, E.I., Borga, M., Creutin, J.D., Marra, F., 2015. Estimation of debris flow triggering rainfall: Influence of rain gauge density and interpolation methods. *Geomorphology* 243, 40–50. URL: <http://dx.doi.org/10.1016/j.geomorph.2015.04.028>, doi:10.1016/j.geomorph.2015.04.028.
- Pastor, M., Blanc, T., Haddad, B., Drempetic, V., Morles, M.S., Dutto, P., Stickle, M.M., Mira, P., Merodo, J.A., 2015. Depth Averaged Models for Fast Landslide Propagation: Mathematical, Rheological and Numerical

- Aspects. *Archives of Computational Methods in Engineering* 22, 67–104. doi:10.1007/s11831-014-9110-3.
- Pirulli, M., 2005. Numerical Modelling of Landslides RunOut. PhD thesis
- Pirulli, M., Bristeau, M.O., Mangeney, A., Scavia, C., 2007. The effect of the earth pressure coefficients on the runout of granular material. *Environmental Modelling and Software* 22, 1437–1454. doi:10.1016/j.envsoft.2006.06.006.
- Pirulli, M., Mangeney, A., 2008. Results of back-analysis of the propagation of rock avalanches as a function of the assumed rheology. *Rock Mechanics and Rock Engineering* 41, 59–84. doi:10.1007/s00603-007-0143-x.
- Pouliquen, O., 1999. Scaling laws in granular flows down a rough plane. *Physics of Fluids* 11, 542–548. doi:10.1063/1.1416884.
- Pouliquen, O., Forterre, Y., 2002. Friction law for dense granular flows: Application to the motion of a mass down a rough inclined plane. *Journal of Fluid Mechanics* 453, 133–151. doi:10.1017/S0022112001006796, arXiv:0108398.
- Premnath, K.N., Abraham, J., 2007. Three-dimensional multi-relaxation time (MRT) lattice-Boltzmann models for multiphase flow. *Journal of Computational Physics* 224, 539–559. doi:10.1016/j.jcp.2006.10.023, arXiv:0611016.
- Pudasaini, S.P., Hutter, K., 2003. Rapid shear flows of dry granular masses down curved and twisted channels. *Journal of Fluid Mechanics* 495, 193–208. doi:10.1017/S0022112003006141.
- Pudasaini, S.P., Wang, Y., Hutter, K., 2005. Rapid motions of free-surface avalanches down curved and twisted channels and their numerical simulation. *Philosophical Transactions of the Royal Society A: Mathematical, Physical and Engineering Sciences* 363, 1551–1571. doi:10.1098/rsta.2005.1595.
- RM Iverson, 1997. The Physics of Debris Flows. *Reviews of Geophysics* 35, 245–296. doi:10.1029/97RG00426;.
- Savage, S.B., Hutter, K., 1989. The motion of a finite mass of granular material down a rough incline. *Journal of Fluid Mechanics* 199, 177–215. doi:10.1017/S0022112089000340.
- Scheidl, C., Chiari, M., Kaitna, R., Müllegger, M., Krawtschuk, A., Zimmermann, T., Proske, D., 2013. Analysing Debris-Flow Impact Models, Based on a Small Scale Modelling Approach. *Surveys in Geophysics* 34, 121–140. doi:10.1007/s10712-012-9199-6.
- Shen, W., Zhao, T., Zhao, J., Dai, F., Zhou, G.G., 2018. Quantifying the impact of dry debris flow against a rigid barrier by DEM analyses. *Engineering Geology* 241, 86–96. URL: <https://doi.org/10.1016/j.enggeo.2018.05.011>, doi:10.1016/j.enggeo.2018.05.011.
- Song, D., Ng, C.W., Choi, C.E., Zhou, G.G., Kwan, J.S., Koo, R.C., 2017. Influence of debris flow solid fraction on rigid barrier impact. *Canadian Geotechnical Journal* 54, 1421–1434. doi:10.1139/cgj-2016-0502.
- Staron, L., Lagrée, P.Y., Popinet, S., 2014. Continuum simulation of the discharge of the granular silo. A validation test for the $\mu(I)$ visco-plastic flow law. *European Physical Journal E* 37, 1:12. doi:10.1140/epje/i2014-14005-6.
- Stolz, A., Huggel, C., 2008. Debris flows in the Swiss National Park: The influence of different flow models and varying DEM grid size on modeling results. *Landslides* 5, 311–319. doi:10.1007/s10346-008-0125-4.
- Succi, S., 2003. *The Lattice Boltzmann Equation for Fluid Dynamics and Beyond*. Oxford University Press, New York. doi:10.1016/S0997-7546(02)00005-5.
- Succi, S., Foti, E., Higuera, F., 1989. Three-dimensional flows in complex geometries with the lattice boltzmann method. *Epl* 10, 433–438. doi:10.1209/0295-5075/10/5/008.
- Tai, Y.C., 2000. Dynamics of granular avalanches and their simulations with shock-capturing and front-tracking numerical schemes. *Shakers Verlag*. URL: <http://ir.lib.ncku.edu.tw/handle/987654321/111504>.
- Tai, Y.C., Noelle, S., Gray, J.M., Hutter, K., 2002. Shock-capturing and front-tracking methods for granular avalanches. *Journal of Computational Physics* 175, 269–301. doi:10.1006/jcph.2001.6946, arXiv:1501.04756.
- Takahashi, T., 2007. *Debris flow Mechanics prediction and countermeasures*. Taylor & Francis, London.
- Trehwela, T., Ancey, C., 2021. A conveyor belt experimental setup to study the internal dynamics of granular avalanches. *Exp. Fluids* 62, 1–17. URL: <https://doi.org/10.1007/s00348-021-03299-0>, doi:10.1007/s00348-021-03299-0.
- Wang, Y., Hutter, K., Pudasaini, S.P., 2004. The savage-hutter theory: A system of partial differential equations for avalanche flows of snow, debris, and mud. Plenary lecture presented at the 81st Annual GAMM Conference, March 24–28, 2003. *ZAMM Zeitschrift für Angewandte Mathematik und Mechanik* 84, 507–527. doi:10.1002/zamm.200310123.
- Wendeler, C., Volkwein, A., Roth, A., Denk, M., Wartmann, S., 2007. Field measurements used for numerical modelling of flexible debris flow barriers, in: *International Conference on Debris-Flow Hazards Mitigation: Mechanics, Prediction, and Assessment, Proceedings*, pp. 681–687.
- Winter, M.G., Heald, A.P., Parsons, J.A., Shackman, L., Macgregor, F., 2006. Scottish debris flow events of August 2004. *Quarterly Journal of Engineering Geology and Hydrogeology* 39, 73–78. doi:10.1144/1470-9236/05-049.
- Winter, M.G., Shearer, B., Palmer, D., Peeling, D., Harmer, C., Sharpe, J., 2016. The Economic Impact of Landslides and Floods on the Road Network. *Procedia Engineering* 143, 1425–1434. URL: <http://dx.doi.org/10.1016/j.proeng.2016.06.168>, doi:10.1016/j.proeng.2016.06.168.
- Wu, T., WH, T., Einstein, H., 1996. *Landslide hazard and risk assessment I*, in: Turner and AK, S.R. (Ed.), *Landslides. Investigation and mitigation*. National Academy Press, Washington. 1969. chapter 6, pp. 106–118.
- Yue, Y., Smith, B., Batty, C., Zheng, C., Grinspun, E., 2015. Continuum foam: A material point method for shear-dependent flows. *ACM Transactions on Graphics* 34. doi:10.1145/2751541.
- Zhan, L., Peng, C., Zhang, B., Wu, W., 2019. Three-dimensional modeling of granular flow impact on rigid and deformable structures. *Computers and Geotechnics* 112, 257–271. URL: <https://doi.org/10.1016/j.compgeo.2019.03.019>, doi:10.1016/j.compgeo.2019.03.019.